Experimental Characterization and Constitutive Modeling of AZ31B and ZEK100 Magnesium alloys for Monotonic and Reverse Loading Paths

by

Waqas Muhammad

A thesis

presented to the University of Waterloo

in fulfillment of the

thesis requirement for the degree of

Master of Applied Science

in

Mechanical Engineering

Waterloo, Ontario, Canada, 2014

Author's Declaration

I hereby declare that I am the sole author of this thesis. This is a true copy of the thesis, including any required final revisions, as accepted by my examiners.

I understand that my thesis may be made electronically available to the public.

Abstract

Finite element (FE) simulations are widely used in automotive design processes to model the forming behavior of sheet metals. Comprehensive material characterization and the availability of suitable constitutive models are prerequisites for accurate modeling of these forming operations. In the current research, monotonic tension, compression and large strain compression-tension-compression (CTC) and tension-compression-tension (TCT) experiments have been performed to characterize the mechanical behavior of AZ31B and ZEK100 magnesium sheets at room temperature. A digital image correlation system is used to measure the surface strains during monotonic tension and compression testing. The data is later processed to calculate the evolution of r-values with plastic deformation. Texture measurements of the annealed materials and fractography of deformed specimens under monotonic tension and compression are also performed. The results of mechanical testing are discussed in light of the crystallographic texture and deformation mechanisms such as slip, twinning and untwinning. It is observed that annealed AZ31B sheet has a strong basal texture where the majority of crystallographic c-axes are aligned in the sheet normal (ND) direction whereas the annealed ZEK100 sheet exhibits a comparatively weak basal texture, with significant basal pole spreading in sheet transverse direction (TD). The AZ31B sheet specimens exhibit higher in-plane flow stresses and lower ductility as compared to ZEK100 sheet specimens. The tension-compression yield asymmetry is found to be more pronounced in AZ31B sheet as compared to ZEK100 sheet. In addition to this, the ZEK100 sheet specimens exhibit a strong in-plane orientation dependency of flow stress when subjected to uniaxial tension. Furthermore, a significantly greater evolution of plastic anisotropy (r-values) is observed for AZ31B sheet specimens as compared to ZEK100 sheet specimens. Moreover, the unusual S-shaped hardening behavior is observed during reverse tension following previous compression portions of CTC and TCT flow curves of AZ31B and ZEK100 sheets.

A constitutive model is also proposed to capture the evolving asymmetric/anisotropic hardening response of magnesium alloys considering both monotonic and reverse loading paths. The hardening behaviour of magnesium alloys is classified into three deformation modes (i.e. Monotonic Loading [ML], Reverse Compression [RT], and Reverse Tension [RT]). The deformation modes correspond to the different loading regimes of the cyclic hardening curve. Specifically, the ML mode corresponds to the initial in-plane tension and the initial in-plane

compression from the annealed state, the RC mode corresponds to the in-plane compression following previous tension and the RT mode corresponds to the in-plane tension following previous compression. A multi-yield surface modeling approach is used where a CPB06 type anisotropic yield surface is assigned to each deformation mode. For each deformation mode, the yielding criterion is modified to capture the evolution of subsequent yield loci with accumulated plastic deformation. A strain rate independent elasto-plastic formulation is used to implement the proposed constitutive model as a UMAT in LS-DYNA. The predictions of the model are compared against the experimental monotonic and cyclic (CTC and TCT) flow stresses of AZ31B and ZEK100 sheets along different test directions. An excellent agreement is found between the simulated and experimental results.

Acknowledgements

First and foremost, I would like to express my sincere gratitude to my supervisor, Professor Kaan Inal, whose expertise, understanding and patience added considerably to my graduate experience. I would like to thank him for encouraging my research and for providing me this valuable opportunity to grow as a research scientist. Professor Kaan Inal was also my undergraduate solid mechanics professor at the University of Waterloo. His teaching style and enthusiasm for the topic made a strong impression on me and it was under his tutelage that I developed a focus and became interested in pursuing a graduate career in solid mechanics. Apart from his academic and technical support, I would like to thank him for his motivation, moral support and kindness throughout the entire process; without him this thesis would not have been completed.

I would also like to express my special thanks to Dr. Jidong Kang from the Natural Resources Canada's CanmetMATERIALS laboratory in Hamilton, Ontario, for his guidance and many helpful discussions. He raised many precious points in our discussions and I hope that I have managed to address several of them here. I must also thank him for allowing me to perform a major portion of the experimental work in CanmetMATERIALS. Here, I would like to acknowledge the kind support and guidance of Mr. Jie Liang from CanmetMATERIALS in performing the experimental work.

A very special thanks goes out to Dr. Raja K. Mishra from General Motors R&D center in Warren, MI for his technical expertise and helpful discussions. I would like to thank him for providing me with a unique opportunity to visit the General Motors R&D center in Warren, MI and for mentoring and guiding me through the process of microstructural analysis. On that note, I would also like to acknowledge the experimental support and guidance of Mr. Robert Kubic from General Motors R&D center in Warren, MI, in performing the microstructural EBSD analysis.

I would also like to thank all my colleagues at the University of Waterloo for their support throughout the entire process. I would like to take the time and offer my deepest appreciation to Dr. Mohsen Mohammadi for his motivation, encouragement, friendship and countless helpful discussions on my thesis. I would also like to thank Dr. Abhijit Brahme for his helpful comments and guidance with microstructure analysis. The advice and helpful comments of Dr. Dariush Ghaffari Tari and Mr. Usman Ali are also highly appreciated.

Most importantly, I would like to offer my profound and eternal gratitude to my beloved parents for all the sacrifices that you've made on my behalf. Your prayers for me was what sustained me thus far. I would also like to thank all of my friends who supported me in striving towards my goal.

Dedication

To family and friends

Table of Contents

List of Figures

List of Tables

Chapter 1: Introduction

In light of volatile fuel prices and tighter emission regulations by the government, automotive industry has been increasingly considering the use of lightweight materials for structural components. Magnesium (Mg) alloys being the lightest of all possible structural engineering metals, are attractive candidates for use in automotive applications. Magnesium alloys possess low density, superior specific tensile strength and rigidity compared to traditional steel and aluminum alloys (Reed-Hill and Robertson [1957], Roberts [1960], Avedesian and Baker [1999]).

The first use of magnesium alloys in automotive industry is dated back to the Second World War era (Bettles and Gibson [2005]). Currently, the majority of magnesium parts used in automotive applications are die casted (see Figure 1). However, the die casted magnesium parts often have poor fatigue strength and ductility (Doege and Dröder [2001], Xu et al. [2007]). Sheet forming of magnesium alloys, on the other hand, typically exhibit superior mechanical properties such as tensile and fatigue resistance (Duygulu and Agnew [2003], Bettles and Gibson [2005], Agnew et al. [2006], Easton et al. [2006], Jain and Agnew [2007]). However, sheet metal forming of magnesium alloys has been limited due to their poor formability at room temperature (Avedesian and Baker [1999]). The formability of magnesium alloys improves at higher temperatures but warm forming requires more complex tooling setup; thereby increasing the cost of the forming operation.
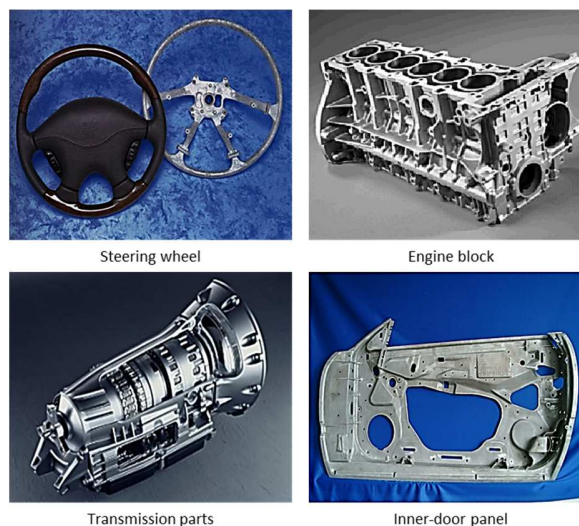
Figure 1: Die cast magnesium parts in automotive industry (Kainer et al. [2008])

Magnesium alloys exhibit unique mechanical properties such as tension-compression asymmetry in flow response and high in-plane anisotropy of yield stress and plastic flow. This unusual mechanical behaviour has been mainly linked to deformation twinning, which is more prevalent at room temperature. Of particular interest is to predict the deformation behavior of these alloys during sheet metal forming processes using finite element modeling (FEM). Due to their unique mechanical behaviour, modeling of magnesium alloys requires careful experimental characterization as well as advanced constitutive laws to predict the deformation behaviors under complex strain path changes during sheet metal forming.

The general goal of this research is to support the application of magnesium alloys for sheet metal forming in automotive industry. In particular, a comprehensive material characterization study of AZ31B and ZEK100 magnesium alloys is conducted to improve the understanding of different deformation mechanisms and their effects on room temperature mechanical behavior of magnesium alloys. Furthermore, a continuum based constitutive model is developed and implemented in a commercial finite element code LS-DYNA to model the complex hardening behaviors of these magnesium alloys.

The remainder of this thesis has been divided into different chapters. Chapter 2 provides background information about different deformation mechanisms in magnesium alloys as well as their effects on formability and mechanical behavior. A brief overview of different modelling approaches till-date is also provided in this chapter. Chapter 3 outlines the main objectives of this research. Chapter 4 details the procedures for experimental analysis. Chapter 5 presents the results of experimental work. The development of the new constitutive model is described in Chapter 6 and its numerical implementation into the FEM code is outlined in Chapter 7. In Chapter 8, the simulation results using the proposed constitutive model are compared with the corresponding experimental findings. The section also summarizes the limitations of the current modelling approach and opportunities for future work. The last chapter of this thesis summarizes the present work and highlights the important observations and conclusions.

Chapter 2: Background

2.1 Deformation mechanisms and formability

Magnesium and its alloys have a hexagonal close-packed (HCP) crystal structure (see Figure 2) with a c/a ratio of 1.624 (Barrett [1952]). The low formability of Mg alloys arises from the limited number of active slip systems at room temperature. Basal $\langle a \rangle$ slip systems are the dominant slip systems in Magnesium alloys at room temperature (Roberts [1960]). Although, other slip systems, such as prism $\langle a \rangle$ and pyramidal $\langle a \rangle$ are also observed in magnesium, their critical resolved shear stresses (CRSS) are generally much higher than those of basal slip systems (Kelley and Hosford [1968b], Obara et al. [1973], Lou et al. [2007], Knezevic et al. [2010]). In order to achieve an arbitrary homogenous deformation in a polycrystalline material, five independent slip systems are required to be activated (Von Mises [1928], Taylor [1938]). However, all the previously mentioned slip systems can only provide a total of four independent slip systems at room temperature. The pyramidal $\langle c + a \rangle$ slip systems, which in principle can provide the additional degree of freedom required for homogeneous deformation, are difficult to activate at room temperature due to their high CRSS (Yoo et al. [2002], Agnew and Duygulu [2005], Lou et al. [2007]). However, it is observed that at room temperature, twinning can provide this additional independent deformation mechanism to satisfy the Von Mises criterion (Kocks and Westlake [1967]).

Unlike dislocation slip, twinning in Mg alloys is a polar mechanism (Agnew and Duygulu [2005]). Two common twinning modes: $\{10\bar{1}2\}\{\bar{1}011\}$ extension twins and $\{10\bar{1}1\}\{10\bar{1}2\}$ contraction twins, have been observed in Mg alloys (Yoo [1981], Knezevic et al. [2010]). The extension twins cause extension of the hexagonal lattice along the crystallographic c direction and reorient the crystal lattice by 86.3° about $\langle 11\bar{2}0 \rangle$ directions. Contraction twins, on the other hand, produce a contractile strain along the crystallographic c direction and reorient the crystal lattice by 56.2° about the same $\langle 11\bar{2}0 \rangle$ directions. (Knezevic et al. [2010]).
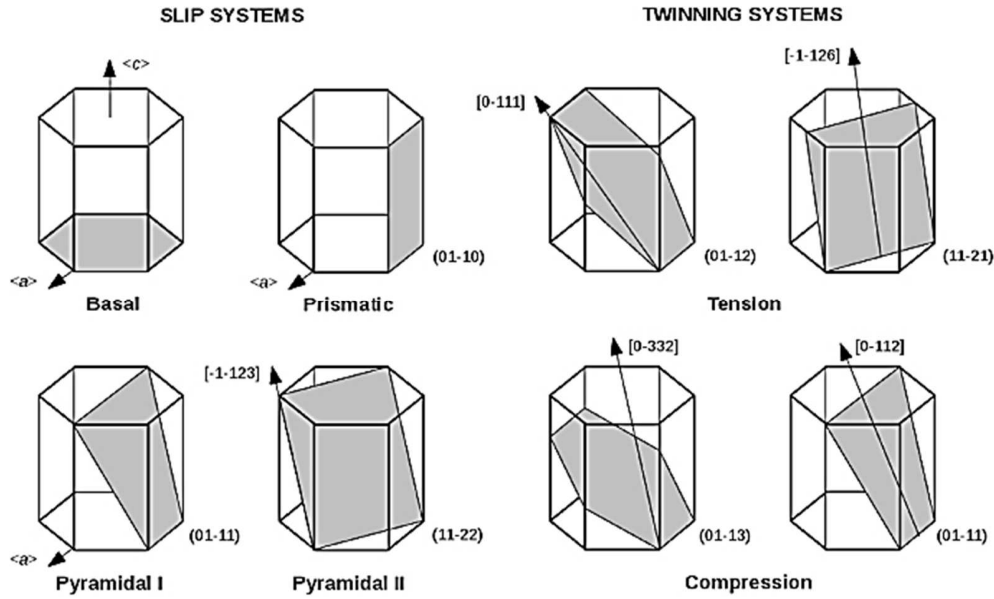
Figure 2: Important slip and twinning systems in magnesium alloys (Luque et al. [2013])

2.2 Initial texture and mechanical behavior

The mechanical properties of magnesium alloys can vary significantly depending on the initial texture and loading path. Metal forming processes such as rolling can induce strong textures in wrought magnesium alloys. A well-known example of this is the AZ31B magnesium sheet, which usually has a strong basal texture developed due to prior rolling (Kaiser et al. [2003], Barnett et al. [2004], Styczynski et al. [2004]), where the majority of grains have their c-axes aligned parallel to the sheet normal direction (ND) (Yukutake et al. [2003], Agnew and Duygulu [2005]). Thus, in-plane tension or through-thickness compression of the sheet causes contraction along the c-axes of majority of the grains. This compressive strain along the c-axes cannot be accommodated by means of easy to activate $\langle a \rangle$ type dislocation slip and require the activation of pyramidal $\langle c + a \rangle$ slip systems or $\{10\bar{1}1\}\{10\bar{1}2\}$ contraction twins (Yoo [1981], Yi et al. [2006], Knezevic et al. [2010]), which are much harder to activate at room temperature due to their high CRSS (Yoo [1981], Gall et al. [2013]). On the contrary, in-plane compressive loading results in extension of the c-axes of the lattice. This tensile strain along the c-axes can be accommodated by easily activated $\{10\bar{1}2\}\{\bar{1}011\}$ extension twinning at room temperature (Agnew and Duygulu [2005]). This strong dependence of deformation mechanisms on the in-plane loading direction of AZ31B sheet, leads to a strong tension-compression yield asymmetry at room temperature. (Gall et al.

[2013]). In addition to this, the limited formability of AZ31B sheet has also been linked to the strong basal texture, which offers only a limited number of active slip systems at room temperature (Agnew and Duygulu [2005], Lou et al. [2007]).

One of the suggested methods to improve the room temperature formability of Mg alloys is by modifying the alloying composition by addition of Rare-Earth (RE) elements such as cerium (Ce), neodymium (Nd), yttrium (Y) and gadolinium (Gd). The addition of RE elements have shown to weaken the basal texture of rolled Mg alloys (Bohlen et al. [2007], Hantzsche et al. [2010], Al-Samman and Li [2011], Jiang et al. [2011]), resulting in an enhancement of formability at room temperature (Dreyer et al [2010], Kurkuri et al. [2014]). Bohlen et al. [2006] has examined the texture and anisotropy of several Mg-Zn-RE alloys with different levels of zinc and rare earth additions. It is reported that the alloying additions has weakened the basal texture by placing more grains in favourable orientations for basal slip and tensile twinning and has also resulted in Lankford coefficient (r-values) of closer to unity. It is suggested that the lower r-values should lead to an improvement in forming behavior, especially under straining conditions, which call for thinning of the sheet (Bohlen et al. [2006]).

Deformation twinning can significantly influence the in-plane hardening response of wrought Mg alloys (Lou et al. [2007], Knezevic et al. [2010]). The compressive hardening behavior of Mg sheet is characterized by an S-shaped sigmoidal hardening curve exhibiting a low initial yield stress (i.e. approximately one half of that for in-plane tension (Nobre et al. [2002]) followed by a concave-up stress-strain behavior with a low initial hardening rate due to extension twinning (Yukutake et al. [2003]). At large compressive strain, due to the exhaustion of twinning and dominance of slip mechanisms, the stress strain curve switches to that of a typical concave-down shape (Yukutake et al. [2003], Lou et al. [2007]). Apart from slip and twinning, untwinning may occur in a previously twinned material and can be characterized by the disappearance of existing twin bands (Lou et al. [2007]). Untwinning can occur during reverse loading paths such as in-plane tension following previous in-plane compression and results in an inflected S-shaped flow curve similar to that of twinning (Lou et al. [2007], Wu et al. [2008]). In cyclic loading of Mg alloys at room temperature, twinning and untwinning appear alternately and leads to a large asymmetry of cyclic deformation (Lou et al. [2007], Lee et. al [2008]). The asymmetric loading reversals and the

Bauschinger effect (Bauschinger [1886]) are often found to become more significant with an increase in strain amplitudes (Xiong et al. [2013]).

2.3   Constitutive modelling

Finite element (FE) simulations are widely used in automotive design processes to predict the deformation behavior of sheet metals during forming processes (Chung et al. [1992], [1996]). The availability of accurate numerical models is critically important for successful numerical analysis. However, due to the unusual mechanical behavior of magnesium alloys, constitutive modeling of these alloys is a challenging task. Several polycrystal type models have been proposed to model the complex deformation behavior of HCP metals (Tomé et al. [1991], Lebensohn and Tomé [1993], Kalidindi [1998], Staroselsky and Anand, [2003], Tomé´ and Lebensohn [2004], Mayeur and McDowell [2007]). Although, the recent development in polycrystal modelling (Proust et al. [2009], Izadbakhsh et al. [2011], Wang et al. [2012,2013b]) has made it possible to capture and study the complex deformation mechanisms in HCP materials, the use of such models for sheet forming applications may still be impractical due to the high computational time. On the other hand, conventional continuum based models (Von Mises [1928], Hill [1948,1950], Hosford [1972], Barlat et al. [1991,1997,2003]) are more suitable for metals with BCC and FCC lattice structures where the mechanical behavior is not influenced by deformation twinning.

Several continuum based approaches have been used to model the tension/compression asymmetry associated with HCP materials by introducing eccentricity of the yield surface (Lee and Backofen [1965], Kelley and Hosford [1968a]). Noticeably, Cazacu and Barlat [2004] modified the Drucker's isotropic yield surface model (Drucker [1949]) to incorporate a strength differential parameter to account for tension/compression asymmetry. The yield surface was further modified to orthotropy by performing linear transformations on the Cauchy stress tensor. Cazacu and Barlat [2006] proposed an orthotropic yield criterion (CPB06) to account for both the anisotropy of a material and the yielding asymmetry between tension and compression. The yield surface was expressed in terms of the principal values of the linearly transformed stress deviator ensuring insensitivity to the hydrostatic pressure. Plunkett et al. [2008] introduced multiple linear transformations to CPB06 and showed that an improved accuracy in both the tensile and compressive anisotropy in yield stresses and r-values of materials could be achieved by

incorporating additional linear transformations of the stress deviator. A different approach was used by Yoon et al. [1998], where a constant non-zero back stress was used to model the initial yield eccentricity of the yield surface. Li et al. [2010] modified the previous approach by introducing evolving Armstrong–Frederick-like (Armstrong and Frederick [1966]) back stress terms to model the evolving tension/compression asymmetry of AZ31B Mg sheets.

Fewer continuum phenomenological approaches have been proposed to describe the reverse loading behavior of magnesium alloys. Lee et al. [2008] used a two surface plasticity model with use of gap functions to describe the reverse hardening behavior. The anisotropy and asymmetry in tension and compression was represented by a modified Drucker-Prager type yield criterion. Li et al. [2010] proposed a phenomenological model TWINLAW, where an isotropic Von Mises type yield surface with an evolving back stress was used to model reverse loading behavior. A set of different kinematic hardening rules depending on the active deformation mode (slip, twinning, and untwinning) were used to model hardening within each deformation mode. Kim et al. [2013] modeled the temperature-dependent asymmetric cyclic behavior of magnesium alloy sheets by classifying the hardening behavior in to three deformation modes based on the dominant deformation mechanism (i.e. twinning , untwinning and slip). The yield surface, at any instant, was defined by two separate yield functions that correspond to the twinning/untwinning and slip dominant deformation modes. Nguyen et al. [2013] has proposed a multi-yield surface modelling approach where the hardening behavior of magnesium sheet was divided in to three deformation modes (slip, twinning, untwinning). Three separate Von Mises yield surfaces (one corresponding to each deformation mode) along with a set of corresponding hardening equations for each deformation mode, were used to model the cyclic hardening behavior of AZ31B sheets.

Texture evolution in magnesium alloys causes evolving tension/compression asymmetry, evolving flow stress anisotropy between the different in-plane loading directions and significant r-values evolution with plastic deformation. This leads to a continuous change in the shape of the yield surface with on-going plastic deformation, which cannot be captured by simple isotropic hardening of the yield surface. Plunkett et al. [2006] proposed a methodology to account for this evolving anisotropy in HCP metals, where evolution of the anisotropic coefficients involved in the expression of the CPB06 yield function (Cazacu and Barlat [2006]) was considered. The yield surface corresponding to an arbitrary equivalent plastic strain level was obtained by interpolating

7

between two previously calibrated yield surfaces. Similar approach was later used by Gilles et al. [2011] to model the evolution of anisotropic hardening in TA-6 V titanium alloy. Yoon et al. [2013] and Ghaffari Tari et al. [2013] used the CPB06 yield criterion along with a set of evolution laws for the anisotropic coefficients involved in the yield criterion expression to model evolving anisotropy in AZ31B sheets.

2.4 Need for current research

Although there has been many material characterization studies performed on magnesium alloys in recent years, most of them have been focusing on the monotonic loading behavior of these alloys. There is limited data available on the large strain cyclic behavior and the evolution of plastic anisotropy in these materials which is required for accurate modeling of forming processes. Apart from material characterization, very few modelling approaches has been proposed to capture the large strain cyclic behavior of magnesium alloys. Furthermore, all the preceding modelling approaches for evolving anisotropic hardening of the yield surface were limited to monotonic loading conditions. To the best of author's knowledge, no effort till date has been made to incorporate the effects of evolving anisotropic hardening of the yield surface considering reverse loading paths. However, accurate modelling of the reverse loading behavior is important as it is usually observed in sheet metal forming applications, when sheet element moves through the tool radii and draw beads (Lee et al. [2008]). Additionally, it is also essential for precise prediction of sheet springback.

Chapter 3: Research Objectives

The overall goal of this research is the development of a rate-independent continuum based plasticity model for large strain cyclic hardening behavior of magnesium alloys. However, in order to achieve this overall goal, two primary objectives are defined as follows

1. Characterization of the quasi-static room-temperature mechanical behavior of AZ31B and ZEK100 magnesium alloy sheets under monotonic and reverse loading paths.

To this end, a comprehensive experimental investigation of the quasi-static, mechanical response of AZ31B and ZEK100 magnesium sheet alloys at room temperature, is presented. The effects of initial texture and different deformation mechanisms on the observed mechanical response of these alloys are also highlighted. Monotonic tension and compression tests are conducted along different in-plane directions and the evolution of r-values is measured as the deformation proceeds. Large strain compression-tension-compression (CTC) and tension-compression-tension (TCT) tests are conducted to characterize the in-plane cyclic hardening behavior.

2. Develop a continuum based constitutive model to capture the evolving asymmetric / anisotropic hardening response of magnesium alloys considering both monotonic and reverse loading paths.

For this purpose, a phenomenological model is proposed in which the cyclic hardening behaviour is classified into three deformation modes (i.e. Monotonic Loading [ML], Reverse Compression [RT], and Reverse Tension [RT]). In contrast to previous research works, the developed model captures the evolving asymmetric/anisotropic response of both flow stresses and r-values under both monotonic and reverse loading conditions. A strain rate independent elasto-plastic formulation is used to implement the proposed constitutive model as a user material subroutine (UMAT) within the commercial finite element software LS-DYNA. For validation of the constitutive model, the predictions of the model are compared against the experimental monotonic and cyclic (CTC and TCT) flow responses of AZ31B and ZEK100 sheets along different test directions.

Chapter 4: Material Characterization - Experimental Procedures

Uniaxial tension, uniaxial compression, and cyclic tension-compression tests were performed to characterize the mechanical behavior of AZ31B and ZEK100 magnesium alloy sheets. All the mechanical tests were conducted at room temperature within the quasi-static regime and were repeated at least three times to ensure good repeatability. Electron Backscatter Diffraction (EBSD) method was used to characterize the initial annealed texture of the starting materials.

4.1   Material properties

AZ31B and ZEK100 alloy sheets with a nominal thickness of 1.6 mm were used in the present study. The chemical compositions of these alloys are listed in Table 1.

<div align="center">Table 1: Chemical composition of as-received AZ31B and ZEK100 sheet materials.</div>

Material	Chemical Composition (Max. wt%)										
	Mg	Al	Zn	Mn	Ca	Cu	Fe	Ni	Si	Zr	Re*
AZ31B	Bal	3.5	1.3	1.0	0.04	0.05	0.005	0.005	0.05	-	-
ZEK100	Bal	-	1.5	-	-	0.008	0.004	0.001	-	0.5	0.22

The as received sheet materials were subjected to annealing heat treatments to eliminate the effects of previous cold working and to obtain a recrystallized starting microstructure. The AZ31B sheet was annealed at 350 °C for 1 h and then air cooled to room temperature. The ZEK100 sheet was annealed at 450 °C for a duration of 1 h in a vacuum furnace with Ar gas protection and then furnace cooled to room temperature. The furnace heating ramp-up rate was set to 100 °C/h for both annealing heat treatments.

4.2   Monotonic tension tests

Sub-sized ASTM tensile specimens (ASTM-E8M-13a) with a gauge length of 25 mm and a gauge width of 6 mm were prepared for tensile testing of AZ31B. The uniaxial tension tests for ZEK100 sheet material were performed using a modified ASTM-E8M sheet specimen with a reduced gauge length of 15 mm (see Figure 3). All the specimens were machined parallel to the rolling direction (RD), transverse to the rolling direction (TD) and 45° to the rolling direction (DD). The tests were carried out using an Instron 8511 Servohydraulic machine with a load cell capacity of 40 KN and

an MTS (Model: 632.12C-21) extensometer. The testing was conducted at room temperature at a nominal strain rate of 5 x 10^{-4}/s.
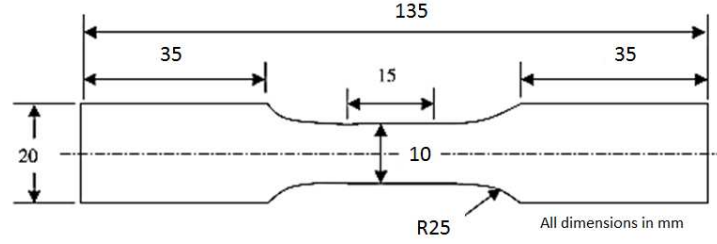
Figure 3: ZEK100 tensile test specimen

The tensile Lankford parameter (r-value) and its evolution with plastic strain was also measured. For this purpose, a digital image correlation (DIC) system ARAMIS® was used to record the sample surface strain with tensile deformation. A random color pattern was sprayed on the sample surface within the gauge length prior to performing the tests. A digital image of the deformation was captured every second for the entire duration of a tensile test and the data was further processed to obtain axial and width strains. The measured axial and width strains were used to calculate r-values as follows:

$$r = \frac{\varepsilon_w^p}{\varepsilon_t^p} = -\frac{\varepsilon_w^p}{\varepsilon_l^p + \varepsilon_w^p} \tag{1}$$

where ε_l^p, ε_w^p and ε_t^p are the axial, width and through-thickness plastic strains respectively. It is noted that the assumption of volume constancy during plastic flow is inherent in the above formulation.

4.3   Monotonic compression tests

The quasi-static compression experiments in RD, DD and TD were performed using single sheet specimens (i.e. no bonding of multiple sheets) with a specimen dimensions of 6.0 mm gauge length, 4.0 mm gauge width and 1.6 mm sheet thickness. Compression tests were also performed through thickness of the sheet with the loading normal to the sheet plane (ND). However, for the compression tests in ND direction, specimens were prepared by bonding together three 1.6 mm thick round sheets having a diameter of 19.05 mm. A rather similar approach has been previously used by Tozawa [1978], Maeda et al. [1998], Ghaffari Tari et al. [2013] and Kurkuri et al. [2014].

A high performance adhesive, Master bond SUPREME10HT®, was used to bond the sheet layers together. A small amount of pressure was applied and maintained for 24 hours until the adhesive was completely cured. For improved bonding results, the bonding surface of each sheet was roughened by light machining prior to bonding.

Sheet metals are prone to buckling when subjected to in-plane compression, which makes it difficult to measure the actual stress-strain behavior of the material. Even though, buckling is a geometry dependent phenomenon, the flatness of contact surfaces (i.e. specimen and tooling contact surfaces) and friction between contacts play an important role in defining the onset of buckling. Thus, before testing, the contact surfaces of all the specimens were ground and polished using three different grades (1200, 2400 and 4000 grit) of SiC papers to minimize the effects of friction and to achieve a shiny surface finish.

A custom designed fixture was used to carry out the compression tests. The fixture consisted of two custom made grips, which were attached to the actuator arms of the Instron machine (Figure 4 (a)). Each grip (i.e. top and bottom) had a machined tungsten carbide insert incised in its center (Figure 4 (b)) and the compression specimen was placed on the carbide insert. The carbide insert provided a hard and flat contact surface between the specimen and the tooling. The test machine, the extensometer and the testing conditions (i.e. temperature and strain rate) used for compression tests were the same as that of the uniaxial tension tests. The r-values in compression were also determined using the DIC system.
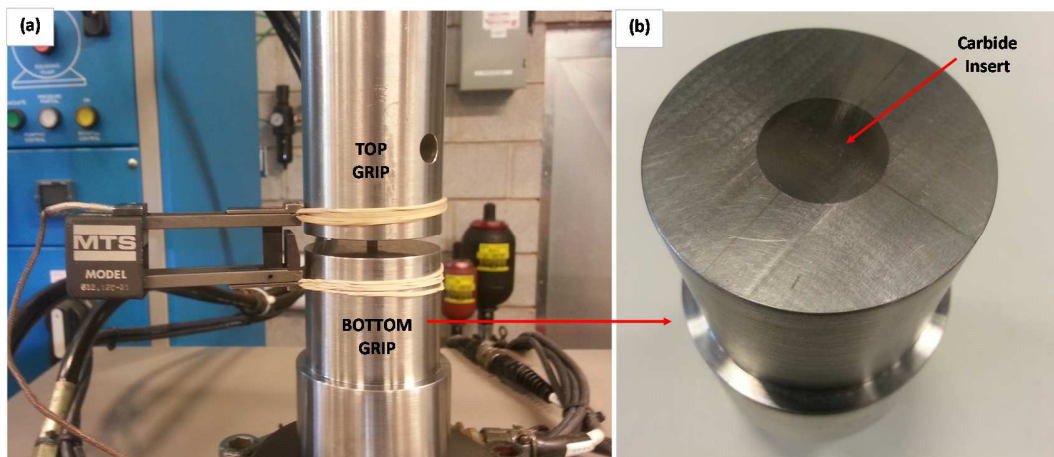
Figure 4: (a) Custom made compression fixture with top and bottom grips and (b) carbide insert incised into the bottom grip

4.4   Cyclic tests

Compression-tension-compression (CTC) and tension-compression-tension (TCT) tests were performed to characterize the in-plane cyclic behavior of AZ31B and ZEK100 alloys. The tests were performed in three (RD, TD and DD) directions for ZEK100 and only in the rolling direction for AZ31B. Various methods have been proposed in the literature to prevent the buckling of specimens during in-plane cyclic compression tests (Kuwabara et al. [1995], Boger et al. [2005], Lou et al. [2007], Piao et al. [2012a,b]). In the present work, an anti-buckling fixture was used to prevent buckling of the sheet specimen during in-plane cyclic compression. The anti-buckling fixture and the cyclic specimen (Figure 5) were a slight modification of the one used by Kim and co-workers in their work (Kim et al. [2013]). The anti-buckling fixture consisted of two machined I-shaped blocks, made of high strength steel and were clamped to the gauge and shoulder portion of the cyclic specimen to prevent the out-of-plane buckling of the specimen. A thin layer of Teflon® sheet was placed between the specimen and the fixture blocks to minimize the effects of friction. The clamping force was adjusted by applying torque to the four bolts connecting the two blocks.
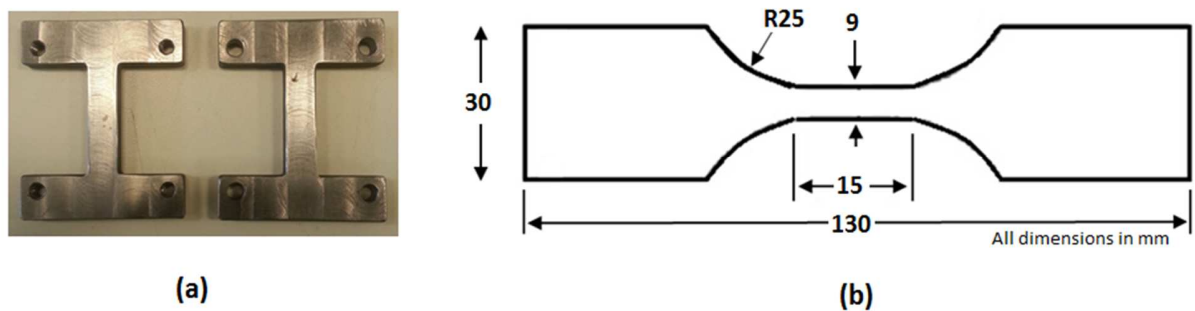
Figure 5: (a) The anti-buckling fixture, (b) the cyclic test specimen

The use of the I-shaped anti-buckling fixture could lead to undesired through thickness stresses imposed on the cyclic specimen. However, it has been reported in the literature that the through thickness stresses caused by the clamping force are negligible as compared to the in-plane stresses, and the amount of stress correction is known to be negligible when an appropriate amount of clamping force is applied (Boger et al. [2005], Kim et al. [2013], Lee et al. [2013]).In addition, before starting a cyclic test, a small amount of load (~0.02 KN) was momentarily applied to the specimen to cause an elastic deformation; and the Young's modulus was measured from the elastic response. This process was repeated and the clamping force on the anti-buckling fixture was

adjusted until the measured Young's modulus was in proximity of the theoretical actual Young's modulus of magnesium. Hence, it was assured that the clamping force was just the proper amount to keep the specimen clamped in place at the beginning of the cyclic test.

The cyclic tests were conducted using an MTS Landmark 370 Servohydraulic machine with a load cell capacity of 100 KN and an MTS (Model: 632.31F-24) extensometer. The tests were performed at room temperature under strain controlled condition at a nominal strain rate of 2.5 x 10^{-4}/s.

4.5   Texture measurements

The EBSD texture measurements were performed for the initial annealed sheet material of AZ31B and ZEK100. The measurements were conducted using a LEO 1450 scanning electron microscope (SEM) equipped with a TSL EBSD camera using a step size of 0.5 µm. The EBSD data was later analyzed using the TSL^{TM} OIM software. The EBSD data was cleaned and only data points having a confidence index (CI) above 0.2 were retained for the analysis.

4.6   Fracture surface characterization

Fracture surfaces of a few representatives samples were examined using (JEOL JSM-6460) scanning electron microscope. Both RD and TD uniaxial tension and compression samples for AZ31B and ZEK100 were examined to reveal fracture mechanisms.

Chapter 5: Material Characterization - Experimental Results and Discussion

5.1   Initial texture

Figure 6 (a) shows the inverse pole figure (IPF) map corresponding to the top rolled surface of the annealed AZ31B sheet. A strong initial basal texture is evident and is consistent with the {0001} basal pole figure (Figure 6 (b)), which shows the majority of c-axes being aligned normal to the sheet plane. However, there is a relatively higher angular spreading of the basal poles towards RD, thereby giving rise to an ellipsoidal intensity distribution of the {0001} pole figure. Furthermore, the prismatic {10$\bar{1}$0} and the pyramidal {10$\bar{1}$1} planes are distributed rather randomly in the sheet plane.
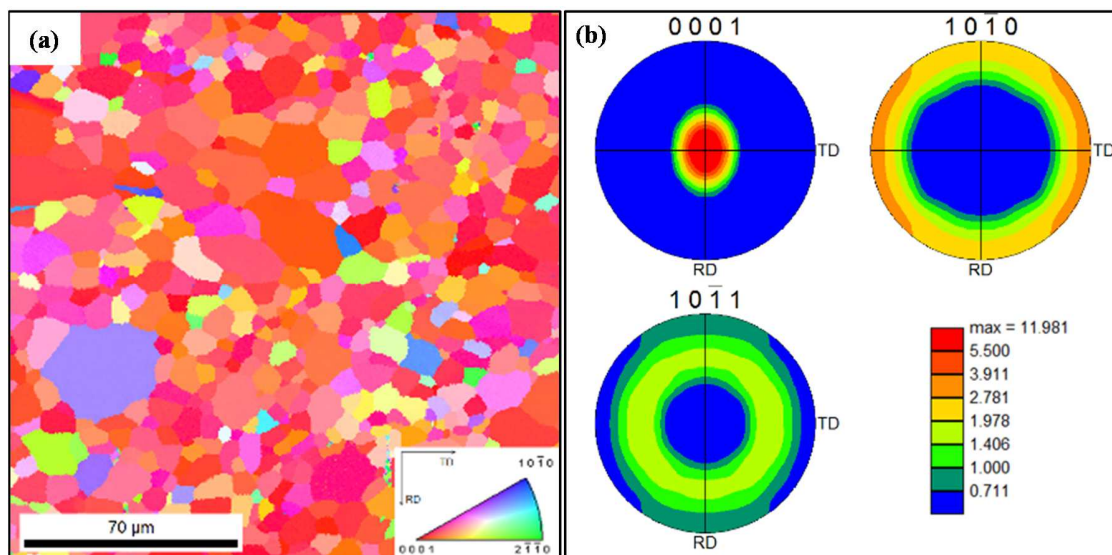
Figure 6: (a) Initial texture and (b) pole figures for annealed AZ31B sheet. The RD-TD plane represents the rolled surface of the sheet.

Figure 7 (a) shows the IPF map of the top rolled surface of the annealed ZEK100 sheet. The IPF map shows grains of several different colors distributed randomly, indicative of the fact that the starting texture for ZEK100 is rather different from that of AZ31B. In fact, the annealed ZEK100 sheet exhibits a relatively weak basal texture (Figure 7 (b)), with significant spreading of basal poles along TD and a weaker peak intensity as compared to that of annealed AZ31B sheet. The intensity distribution for prismatic {1010} planes shows higher intensity along RD whereas the

pyramidal $\{10\bar{1}1\}$ planes appear to be distributed rather randomly in the TD-RD plane with a slightly higher intensity at appropriate angles away from TD towards RD (see Figure 7 (b)).
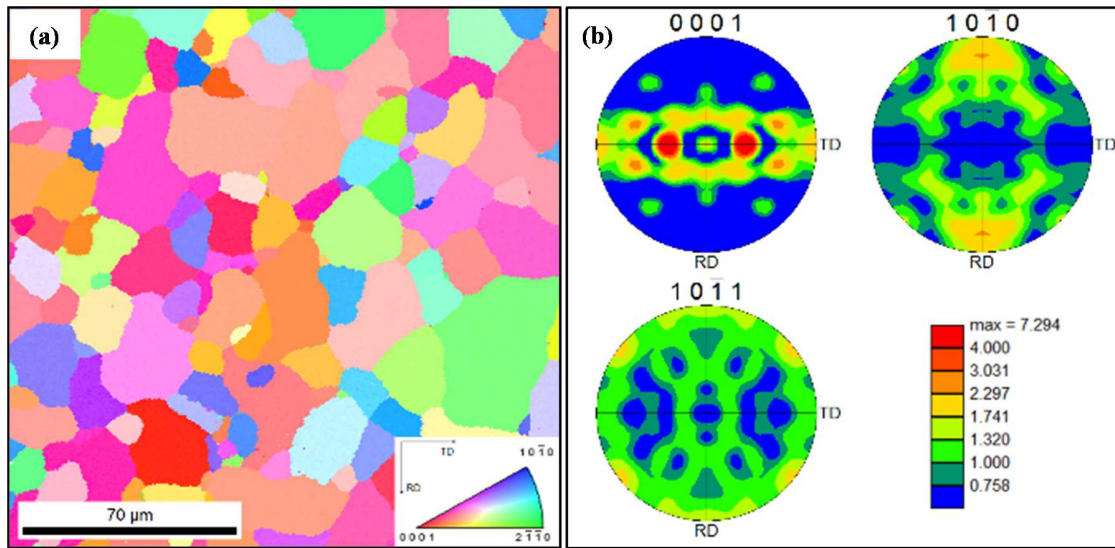
Figure 7: (a) Initial texture and (b) pole figures for annealed ZEK100 sheet. The RD-TD plane represents the rolled surface of the sheet.

Figure 8 shows the Schmid factor distribution for different slip systems (i.e. a $\{0001\}\langle 1\bar{2}10\rangle$ basal plane slip system with an a-axis slip direction, a $\{10\bar{1}0\}\langle 1\bar{2}10\rangle$ prismatic plane slip system with an a-axis slip direction, a $\{10\bar{1}1\}\langle 1\bar{2}10\rangle$ first-order pyramidal plane slip system with an a-axis slip direction, and a $\{11\bar{2}1\}\langle \bar{1}\bar{1}23\rangle$ pyramidal plane slip system with a $\langle c+a\rangle$ slip direction) with loading axis along RD,TD and ND. All the Schmid factors were calculated using EBSD results corresponding to the rolled surface of annealed AZ31B and ZEK100 sheets using the TSL^{TM} OIM software.

It is observed that for the annealed AZ31B specimen (Figure 8 (a)) the frequency percentage of crystals having a high Schmid factor (i.e. between 0.4-0.5) for basal slip is greater for loading along RD then TD. In fact, the average Schmid factor for basal slip for loading along RD is $m_{basal}^{RD} = 0.211$ and that for loading along TD is $m_{basal}^{TD} = 0.172$. This is consistent with the initial $\{0001\}$ pole figure of annealed AZ31B (Figure 6 (b)) where the basal poles show a higher angular spread towards RD then TD leading to an ellipsoidal intensity distribution of the $\{0001\}$ pole figure. Moreover, irrespective of the loading axis, the average Schmid factor for basal slip is considerably lower than that for non-basal slip. However, it is important to realize that although the initial texture of AZ31B is suitably oriented for non-basal slip, the CRSS for non-basal slip is

comparatively high at room temperature (Agnew et al. [2003], Barnett [2003], Agnew and Duygulu [2005], Lou et al. [2007], Ulacia et al. [2010]) thereby, limiting non-basal activity at room temperature. In contrast to the annealed AZ31B sheet, it is observed that for the annealed ZEK100 sheet (Figure 8 (b)), the average Schmid factor for basal slip for loading along TD (i.e. $m_{basal}^{TD} = 0.342$) is higher than that for loading along RD (i.e. $m_{basal}^{RD} = 0.256$) and is most likely caused by the higher angular spread of basal poles towards TD in the initial texture of ZEK100.

It is worth noting that the initial texture of ZEK100 is more favorably oriented for basal slip as compared to the initial texture of AZ31B as indicated by the comparatively higher average Schmid factor values for ZEK100. Since basal slip plays an important role in room temperature deformation of Mg alloys, the relatively easy basal glide in ZEK100 could be an important factor contributing to the overall lower flow stresses observed in uniaxial tension and compression tests of ZEK100 as compared to AZ31B.
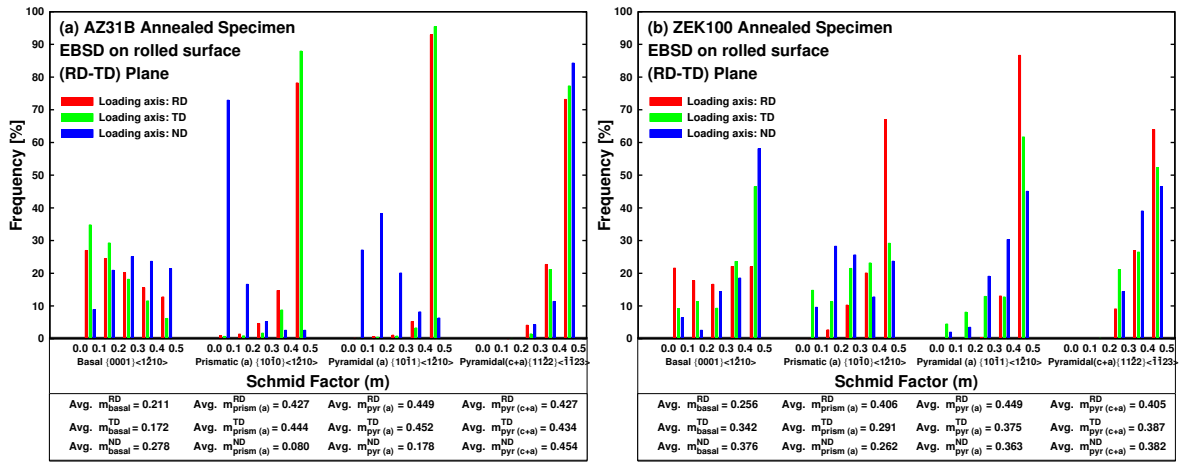
Figure 8: Schmid factor distribution for different slip systems with loading axis along RD,TD and ND for (a) AZ31B annealed sheet and (b) ZEK100 annealed sheet. The Schmid factors are calculated from EBSD results corresponding to the rolled surface of annealed AZ31B and ZEK100 sheets using the TSL^{TM} OIM software.

5.2 Monotonic tension and compression

Figure 9 shows the tensile true stress – true plastic strain curves in the three directions (i.e. RD, DD and TD) for AZ31B and ZEK100 samples tested to failure at room temperature at a nominal strain rate of 5 x 10^{-4} s^{-1}. The corresponding 0.2% offset yield stresses are given in Table 2. The repeatability of the experiments was reasonably good, with an average absolute deviation from the

mean of approximately 2 MPa. The tested specimens showed signs of diffuse necking followed by an abrupt fracture without developing a localized neck, similar to the observations reported by Kang et al. [2013].
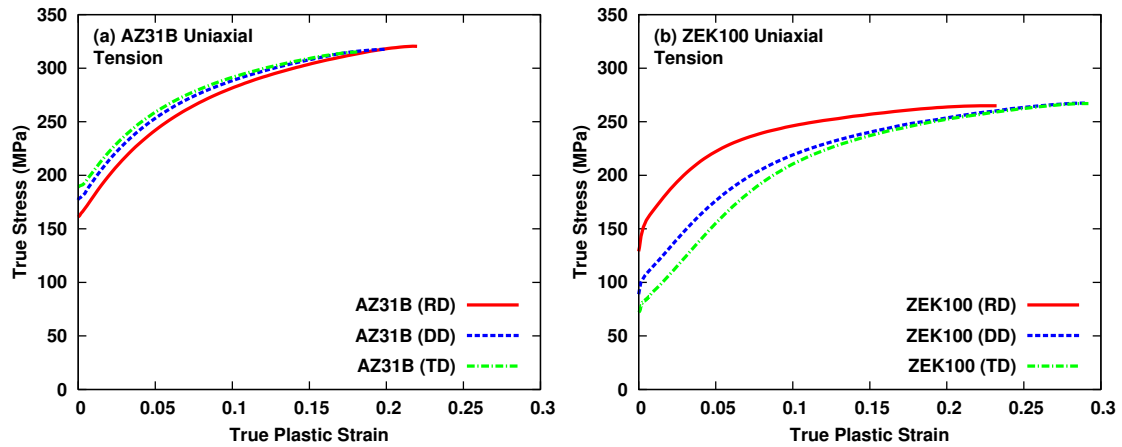
Figure 9: True stress vs. true plastic strain response under monotonic tension for (a) AZ31B and (b) ZEK100

It is observed that for AZ31B sheet specimens (Figure 9 (a)), the stress-strain curves exhibit a concave down shape typical of tensile tests. The yield and flow stresses are highest for TD specimen and lowest for RD specimen, consistent with results reported in the literature (Barnett et al. [2004], Agnew and Duygulu [2005], Lou et al. [2007], Khan et al. [2011]). The lower flow stress in RD as compared to TD is associated with the greater angular spread of basal poles towards RD than TD in the initial AZ31B sheet material (see Figure 6 (b)). This in turn improves the Schmid factor for basal slip for loading along RD (see Figure 8 (a)) leading to relatively easy basal glide and consequently lower flow stress in that direction. The yield and flow stress response for the DD specimen lies in between that of the TD and RD specimens of AZ31B. In general, the tensile stress-strain curves of AZ31B exhibit similar features for loading along the three in-plane directions (i.e. RD, DD, TD). This behavior has been attributed to the inherent in-plane symmetry of the initial basal texture of annealed AZ31B as shown in Figure 6 (b).

In comparison, the uniaxial tension curves for ZEK100 (Figure 9 (b)) exhibit a rather different flow stress response when compared with AZ31B. In particular, the yield and flow stresses are highest along RD and lowest along TD and the difference in yield and flow behavior along the three directions is comparatively more pronounced (i.e. higher planar anisotropy). Furthermore, the flow curve along RD exhibits a typical concave down shape representative of slip dominated deformation whereas the flow curve along TD exhibits an almost linear hardening for the initial

part of tensile deformation with an eventual transition to the concave down shape upon further straining. This linear flow behavior lies in-between that of the slip dominated concave-down and the twinning dominated concave-up behaviors. Similar linear hardening behavior along TD has been reported by Bohlen et al. [2007] in their study on magnesium-zinc-rare earth alloy sheets and by Barnett [2007]. It is suggested that this type of linear hardening behavior is a result of an interaction between basal slip and extension twinning dominated deformation mechanisms Bohlen et al. [2007]. In fact, EBSD texture measurements performed by Kurkuri et al. [2014] on a deformed TD tensile specimen of ZEK100 sheet, have confirmed the occurrence of extension twinning. It has been shown that those grains with their c-axes originally parallel to TD, have been rotated by extension twinning, which resulted in their c-axes to re-orient parallel to RD and ND sheet directions. Kurkuri et al. [2014] has also reported the occurrence of slip on prismatic and pyramidal planes after initial yielding, which is twinning dominated. Together, the occurrence of extension twinning and a mix of basal and prismatic slips may also account for the low strength and higher ductility shown by the TD specimen of ZEK100 as compared to the RD specimen (see Figure 9 (b)).

Figure 10 shows the compressive true stress – true plastic strain curves for AZ31B and ZEK100 sheet specimens tested to failure at room temperature at a nominal strain rate of 5 x $10^{-4}\,s^{-1}$. The corresponding 0.2% offset yield stresses are given in Table 2. The compression test results showed good repeatability with an average absolute deviation from the mean of approximately 6 MPa. The specimens failed by shearing through-thickness of the sheet with no apparent signs of buckling. The fractured surfaces analyzed under SEM showed a typical shear fracture and will be discussed later in this paper.
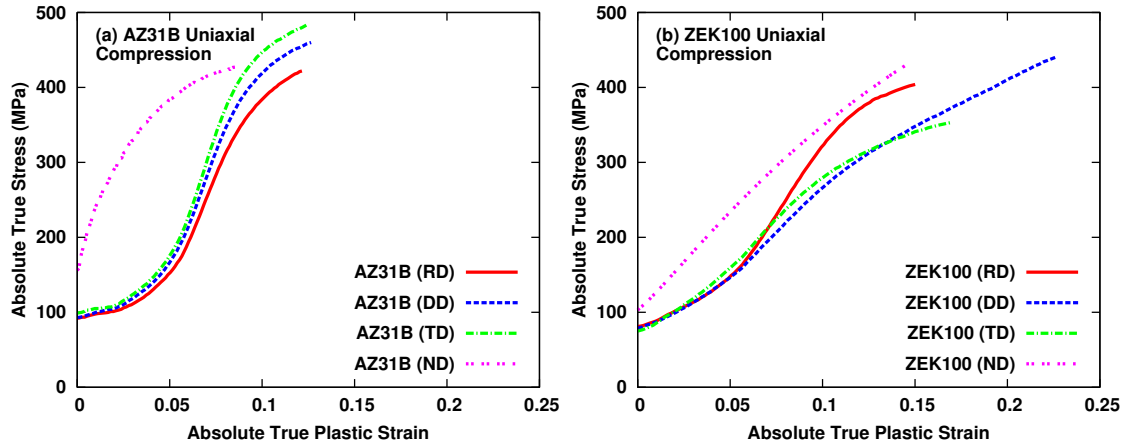
Figure 10: True stress vs. true plastic strain response under monotonic compression for (a) AZ31B and (b) ZEK100

The compression curves for AZ31B and ZEK100 exhibit an unusual concave up appearance up to a certain strain level after which an inflection point is obvious. This behavior is consistent with results reported in literature (Nobre et al. [2002], Barnett et al. [2004], Agnew and Duygulu [2005], Lou et al. [2007]) and has been related to the activation of extension twinning at low strains followed by non-basal slip at larger strains. Consistent with the tensile tests results, the compressive yield and flow stresses for AZ31B are also highest along TD and lowest along RD whereas the contrary is true for ZEK100 sheet specimens. It is also observed that compression of the ND specimen of AZ31B leads to significantly higher flow stress with a typical concave down shape. This behavior is linked to the strong basal texture of AZ31B sheet specimens where the compressive through thickness plastic strain requires contraction along the c-axes of majority of grains. This contraction cannot be accommodated by the means of basal $\langle a \rangle$ and prismatic $\langle a \rangle$ slips; thus, it requires activation of $\langle c + a \rangle$ pyramidal slip and contraction twinning, which consequently leads to higher flow stresses and comparatively lower ductility (Jiang et al. [2007]). Consistent with the recent results reported by Kurkuri et al. [2014], the ND (through-thickness) compression curve of ZEK100 also shows a tendency towards the concave down flow behavior, reflective of a predominant crystallographic slip deformation mechanism.

In general, irrespective of the loading type (i.e. tension or compression), the flow stresses for AZ31B are comparatively higher than the corresponding flow stresses for ZEK100 sheet specimens.

Table 2: 0.2% offset yield stresses for AZ31B and ZEK100

		RD	DD	TD	ND
AZ31B	$\sigma_{0.2\%}^{tension}$ (MPa)	161	177	189	-
	$\sigma_{0.2\%}^{compression}$ (MPa)	92	93	99	156
ZEK100	$\sigma_{0.2\%}^{tension}$ (MPa)	129	89	72	-
	$\sigma_{0.2\%}^{compression}$ (MPa)	81	79	75	103

5.3   Tension-compression asymmetry and planar anisotropy

The yield stress anisotropy ratios given in Table 3 are calculated by dividing the highest in-plane yield stress by the lowest. It is noted that, even though the 0.2% yield stresses (given in Table 2) for AZ31B sheet material used in this study, are slightly lower then what has been previously reported by Lou et al. (2007), the yield stress anisotropy ratios are almost identical. It is also observed that the ZEK100 sheet specimens exhibit a high yield stress anisotropy ratio (i.e. 1.79) when subjected to uniaxial tension. In other words, the uniaxial tensile yield strength for ZEK100 samples oriented along RD is significantly higher than for those oriented along TD. This is related to the initial texture of ZEK100, which shows significant spreading of basal poles in TD, consequently resulting in the activation of extension twinning when subjected to tensile loading along TD. Thus, the activation of extension twinning leads to significantly lower tensile yield stress in TD as compared to RD and accordingly resulting in a relatively high tensile yield anisotropy ratio. It is also worth noting that the compressive yield stress anisotropy ratios for AZ31B and ZEK100 sheet materials are almost identical. This is due to the fact that irrespective of the loading direction (i.e. RD or TD), yielding during in-plane compression is dominated by the activation of extension twinning in both materials.

The yield stress asymmetry is much more pronounced in annealed AZ31B sheet specimens as compared to annealed ZEK100 sheet specimens. As a result, the yield stress asymmetry ratios (Table 3) are noticeably higher for AZ31B sheet specimens. This profound yield stress asymmetry between tension and compression is caused by the strong basal texture of annealed AZ31B, which favours extension twinning only under in-plane compression. Furthermore, the TD specimen of ZEK100 shows almost similar yield strength in tension and compression as reflected by the very low yield stress asymmetry ratio of close to unity (i.e. 0.96 in Table 3). This is because extension twinning is the dominant deformation mechanism in the early stages of both tensile and

compressive plastic deformations in TD. Thus, the tensile and compressive yield strengths of the TD specimen of ZEK100 are fairly identical.

Table 3: Yield stress asymmetry and anisotropy ratios for AZ31 and ZEK100 sheet specimens

Yield stress asymmetry ratio $\left(\dfrac{\sigma_{tension}}{\sigma_{compression}}\right)$				Yield stress anisotropy ratio	
	RD	DD	TD		
AZ31B	1.75	1.90	1.91	$\left(\dfrac{\sigma_{TD}}{\sigma_{RD}}\right)_{tension}$	$= 1.17$
				$\left(\dfrac{\sigma_{TD}}{\sigma_{RD}}\right)_{compression}$	$= 1.07$
ZEK100	1.59	1.13	0.96	$\left(\dfrac{\sigma_{RD}}{\sigma_{TD}}\right)_{tension}$	$= 1.79$
				$\left(\dfrac{\sigma_{RD}}{\sigma_{TD}}\right)_{compression}$	$= 1.08$

5.4 Anisotropy of deformation

The evolution of the Lankford parameter (r-value) with uniaxial deformation was measured using the DIC system (ARAMIS®). Figure 11 shows the evolution of tensile and compressive r-values with true plastic strain for uniaxial tension and compression tests of AZ31B and ZEK100. It is observed that AZ31B (Figure 11 (a),(b)) exhibits significant evolution of plastic anisotropy (r-values) in both tension and compression. The plastic anisotropy evolve much more rapidly for uniaxial tension along TD and is linked with the higher incidence of non-basal $\langle a \rangle$ slip relative to basal $\langle a \rangle$ slip during TD tension (Agnew and Duygulu [2005], Horton et al. [2005b], Lou et al. [2007]). On the other hand, twinning produces substantial amount of through thickness plastic strain and as a result the compressive r-values for AZ31B are less than 1. The compressive r-values show an eventual increase with plastic strain, which is related to the exhaustion of twinning and dominance of slip with continuous compressive plastic straining (Lou et al. [2007]).

22
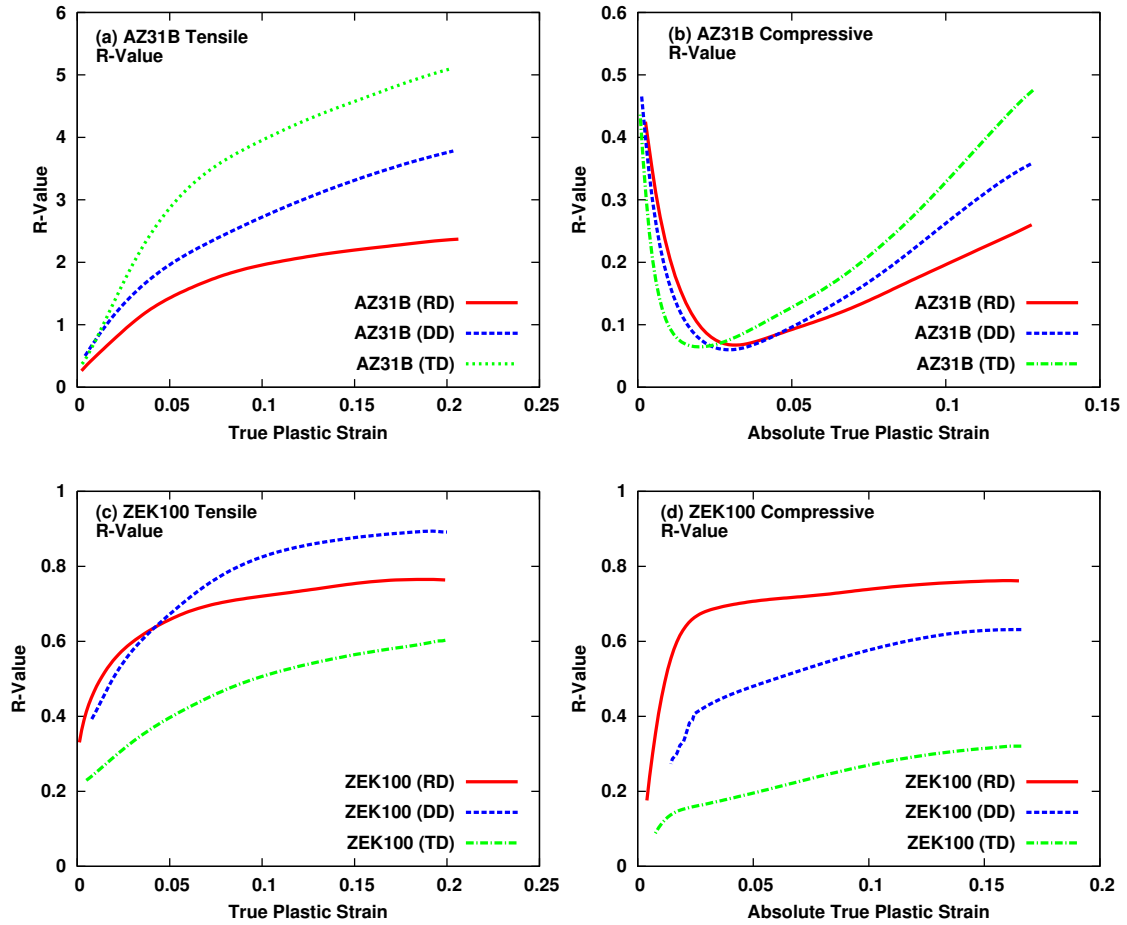
Figure 11: R-values evolution with true plastic strain under monotonic tension and compression for AZ31B and ZEK100

A reduced plastic anisotropy (r~1) is observed for ZEK100 (Figure 11 (a),(b)) as compared to AZ31B. This behavior is related to the weaker basal texture of ZEK100, which has a comparatively large volume fraction of grains oriented favourably to accommodate the in-plane plastic deformation by slip and twinning; thus promoting sheet thinning (Bohlen et al. [2007]). Furthermore, for ZEK100 sheet material, it is observed that irrespective of tensile or compressive loading, the r-values for TD are much lower than those observed for RD and DD test directions. This trend is consistent with the results reported by Kurkuri et al. [2014], where it is suggested that this behavior is associated with greater resistance to in-plane deformation along RD as compared to ND (through-thickness) direction and is a result of the greater angular spreading of basal poles in TD direction of ZEK100 sheet.

5.5 Fractography

Figure 12 shows the fracture surfaces of RD and TD tensile specimens of ZEK100 and AZ31B sheets. The ZEK100 RD and TD specimens show signs of ductile tearing along with the presence of some voids. On the other hand, many small micro voids are visible in the SEM images corresponding to RD and TD specimens of AZ31B. There is also some fast tearing apparent in the SEM images.

Figure 13 shows the fracture surfaces of RD and TD specimens of ZEK100 and AZ31B sheet specimens subjected to monotonic compression. All SEM images show a typical shear fracture surface. The successive striations caused by the shearing force are noticeable in each SEM photomicrograph.
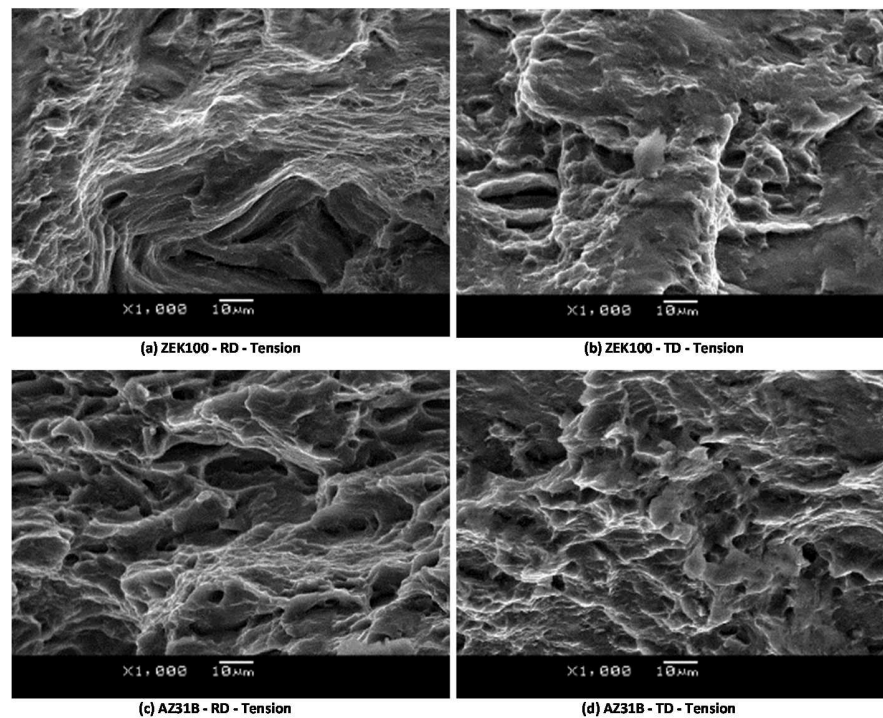
Figure 12: Fracture surfaces of (a) ZEK100 RD (b) ZEK100 TD (c) AZ31B RD and (d) AZ31B TD tensile specimens deformed at a strain rate of 5×10^{-4} s^{-1} at room temperature.
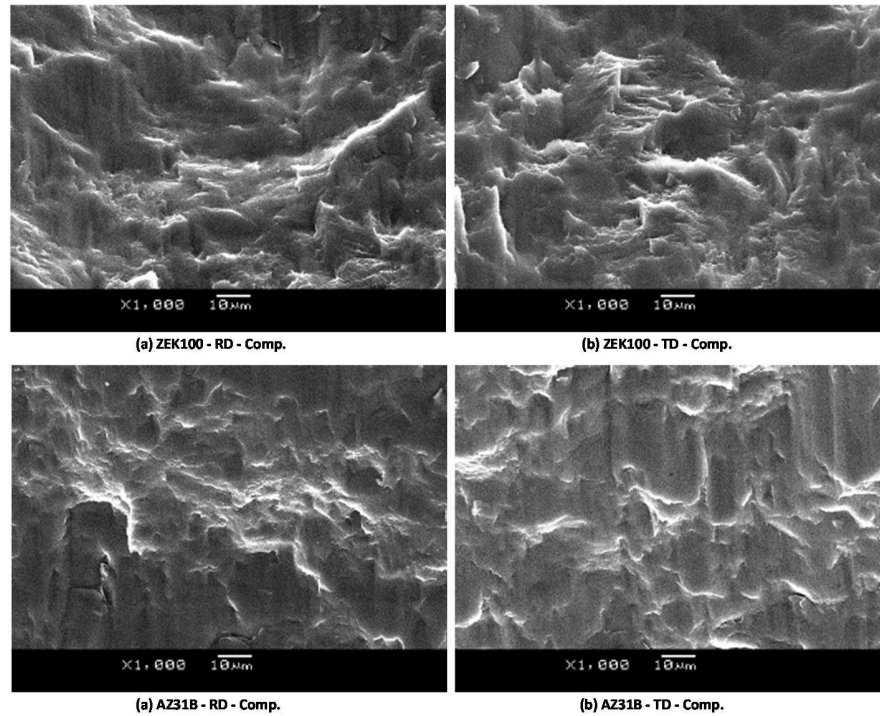
Figure 13: Fracture surfaces of (a) ZEK100 RD (b) ZEK100 TD (c) AZ31B RD and (d) AZ31B TD compression specimens deformed at a strain rate of 5x10^{-4} s^{-1} at room temperature.

5.6   Cyclic CTC and TCT tests

Compression-tension-compression (CTC) and tension-compression-tension (TCT) tests were conducted for AZ31B (Figure 14) and ZEK100 (Figure 15) sheet materials using strain amplitudes of 2%, 4% and 6%. As mentioned previously, the experiments were conducted in all three test directions (RD, DD and TD) for ZEK100 and only in RD for AZ31B mainly due to the fact that a good amount of cyclic data for AZ31B is already available in the literature and the similarity in flow stress evolution across the three test directions has been reported for AZ31B (Lou et al. [2007]).
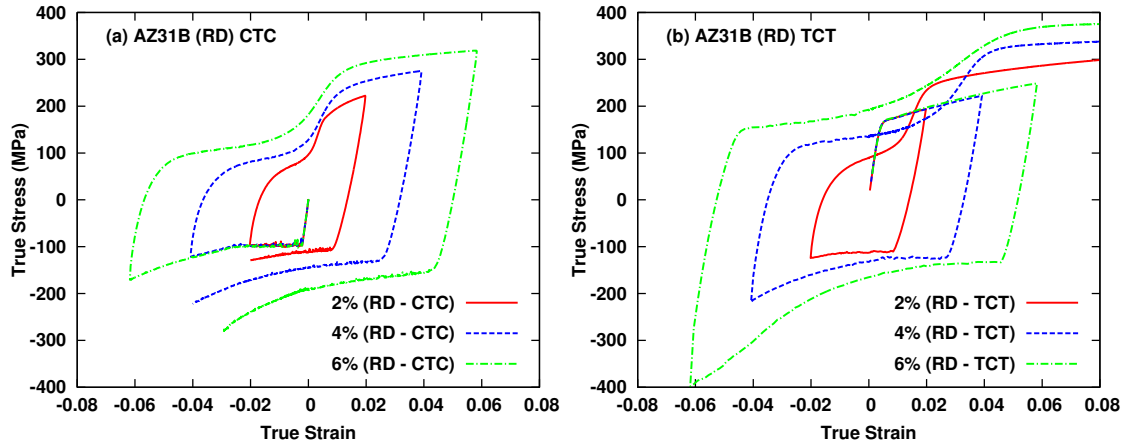
Figure 14: (a) CTC and (b) TCT true stress vs. true strain curves for AZ31B with 2%, 4% and 6% strain amplitudes for loading along RD

With the exception of differences in yield stresses related to textural anisotropy, the flow stresses for AZ31B CTC and TCT tests (Figure 14) are highest for samples oriented along TD and lowest for those oriented along RD whereas the contrary is true for CTC and TCT tests of ZEK100 (see Figure 15). It is also observed that the CTC and TCT curves for AZ31B and ZEK100 exhibit an unusual sigmoidal S-shaped behavior in the reverse tension portion of the deformation following previous compression. This inflected shape does not show up in monotonic uniaxial tension tests or in the initial tensile deformation region of TCT curves. Similar behavior has been previously reported by Lou and co-workers for AZ31B and is linked with the activation of untwinning process which is activated by extension along the *c*-axes of the previously twinned grains (Lou et al. [2007]). It is also observed that this sigmoidal behavior during reverse tension is much more pronounced for ZEK100 samples oriented along RD and least pronounced for those oriented along TD. Lastly, as expected, the reverse tensile and compressive yield stresses for CTC and TCT loadings increase with an increase in strain amplitude from 2% to 6%.

26
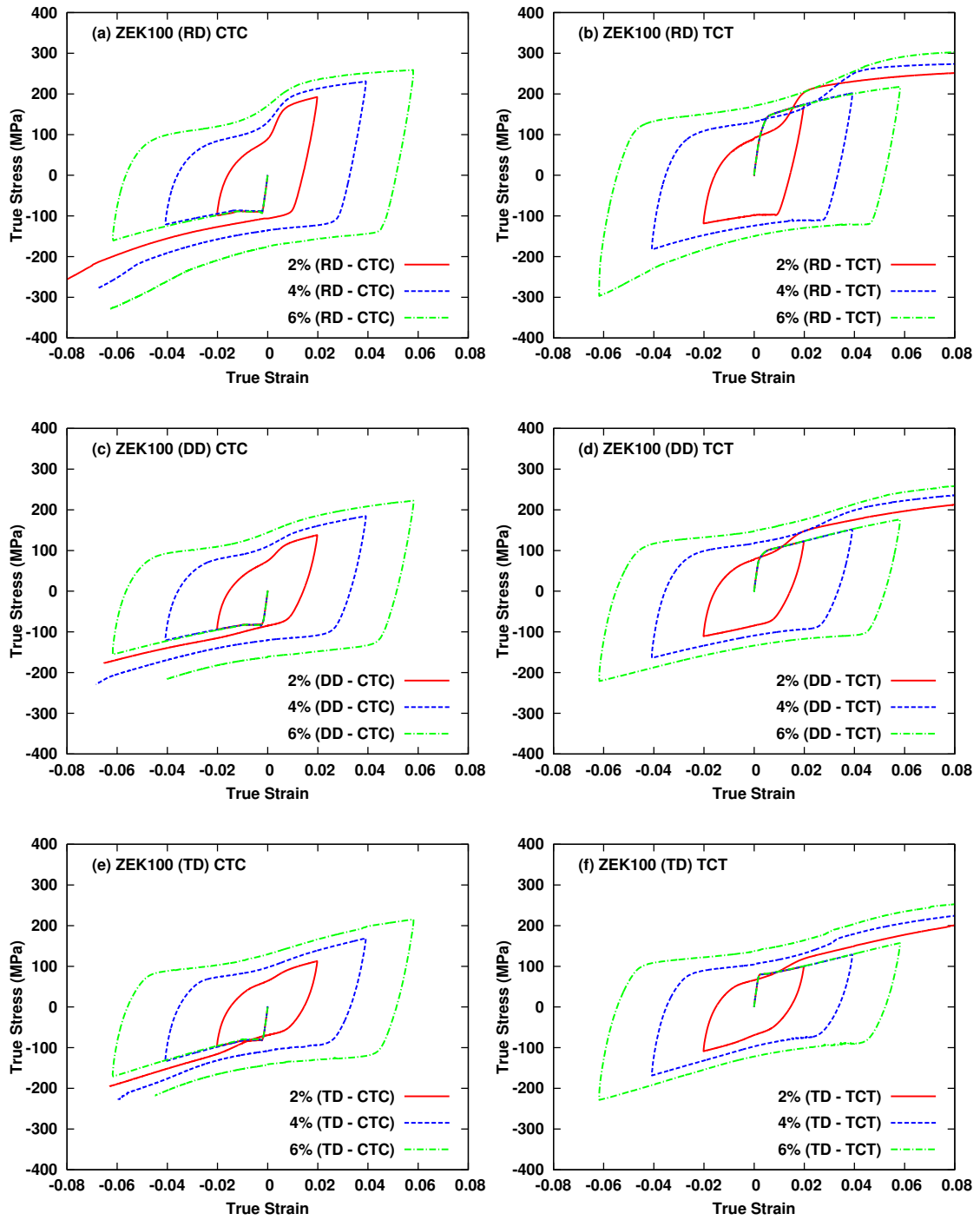
Figure 15: (a),(c),(e) CTC and (b),(d),(f) TCT true stress vs. true strain curves for AZ31B with 2%, 4% and 6% strain amplitudes for loading along RD, DD and TD.

Chapter 6: Constitutive Model Development

6.1   Modelling approach

One of the major goals of this research is to develop a constitutive model that can capture the anisotropic/asymmetric hardening behavior of AZ31B and ZEK100 sheet metals subjected to monotonic or cyclic loading conditions. Several phenomenological continuum plasticity models have been proposed to capture the hardening behavior of AZ31 under reverse loading paths (Lee et al. [2008], Li et al. [2009], Kim et al. [2013], Nguyen et al. [2013]). A general approach is to classify the cyclic hardening behavior into three different deformation modes based on the dominant deformation mechanisms such as "Twinning" during in-plane compression, "Untwinning" during reverse tension and "Slip" during tension from the undeformed state or after exhaustion of twinning or untwinning deformation (see Li et al. [2009], Kim et al. [2013]). This classification of the cyclic hardening behavior is reasonable for some magnesium alloys such as AZ31B since it exhibits a strong basal texture (see Figure 6 (b)), which favors extension twinning deformation only during in-plane compression of the sheet. However, as discussed in the previous section, rare-earth magnesium alloys such as ZEK100 exhibit a comparatively weaker bimodal texture (see Figure 7 (b)); hence, extension twinning can be activated during both in-plane compression and in-plane tension. Consequently, it becomes rather difficult to associate a certain deformation mechanism (i.e. Twinning, Untwinning or Slip) with a certain type of loading (i.e. tension or compression). Therefore, in order to avoid such complications in the current modeling work, a relatively simple but effective approach is proposed.

Figure 16 shows the schematic of typical CTC and TCT curves of a magnesium alloy sheet at room temperature. Four different loading regimes can be identified from the curves namely, initial tension, initial compression, reverse tension following compression and reverse compression following tension. In order to simplify the modeling approach, the cyclic hardening behavior of magnesium alloys is classified in accordance with these different loading regimes. More precisely, three distinct deformation modes are proposed: MODE1 - Monotonic Loading (ML), which corresponds to initial tension and initial compression portion of the CTC and TCT hardening curves. MODE2 - Reverse Compression (RC), which corresponds to the compression following tension portion of the CTC and TCT hardening curves. MODE3 - Reverse Tension (RT), which

corresponds to the tension following compression portion of the CTC and TCT curves (see Figure 16). It is noted that, only one of the three deformation modes can be active at a time. The activation criterion for the three deformation modes is explained next.
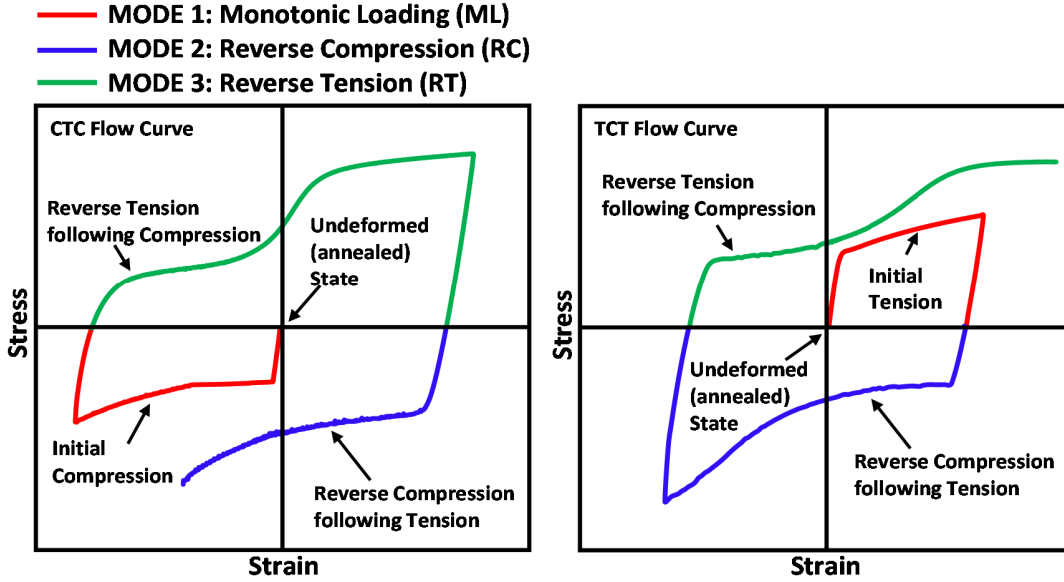
Figure 16: Flow stress curves for the three deformation modes: MODE 1: Monotonic Loading (ML), MODE 2: Reverse Compression (RC) and MODE 3: Reverse Tension (RT).

The Monotonic Loading (ML) is the default deformation mode to begin with. In other words, any loading applied to the initial undeformed state (see Figure 16) will automatically activate this mode. The initial plastic deformation is certain to happen within this mode. However, as to which of the remaining two deformation modes (i.e. Reverse Compression (RC) or Reverse Tension (RT)) will activate next, is linked with the direction of the subsequent reverse loading from ML mode. If the subsequent reverse loading after the initial plastic deformation in ML mode is compressive in nature, it leads to the activation of the RC mode. On the contrary, if the subsequent reverse loading, after the initial plastic deformation in ML mode is tensile, it leads to the activation of the RT mode. Lastly, the RC mode can also become active as a consequence of reverse loading from the RT mode and vice versa. The direction of reverse loading (i.e. whether tensile or compressive) is identified by the sum of the in-plane principal strains increments. This can be formulated as below

$$\text{Direction of reverse loading } = \begin{cases} Tensile \ if & (\Delta\varepsilon_1 + \Delta\varepsilon_2 \ \geq 0) \\ Compressive \ if & (\Delta\varepsilon_1 + \Delta\varepsilon_2 \ < 0) \end{cases} \tag{2}$$

29

where $\Delta\varepsilon_1$ and $\Delta\varepsilon_2$ are the major and minor principal in-plane strain increments respectively and for the plane stress formulation implied in this work,

$$\Delta\varepsilon_{1,2} = \frac{\Delta\varepsilon_{xx} + \Delta\varepsilon_{yy}}{2} \pm \sqrt{\left(\frac{\Delta\varepsilon_{xx} - \Delta\varepsilon_{yy}}{2}\right)^2 + \Delta\varepsilon_{xy}^2} \tag{3}$$

where $\Delta\varepsilon_{xx}$ and $\Delta\varepsilon_{yy}$ are the in-plane normal strain increments and $\Delta\varepsilon_{xy}$ is the in-plane shear strain increment. A criterion for the detection of reverse loading is defined next. For this purpose, an existing criterion for reverse loading has been adapted from the literature (Lee et al. [2008]). Figure 17 shows the schematic representation of the reverse loading criterion, where θ_d represents the relative angle between the two stresses representing the previous $\boldsymbol{d}_{old}$, and the current loading directions $\boldsymbol{d}_{new}$ and θ_r is a prescribed reference angle (i.e. typically set to $\pi/2$) for reverse loading.
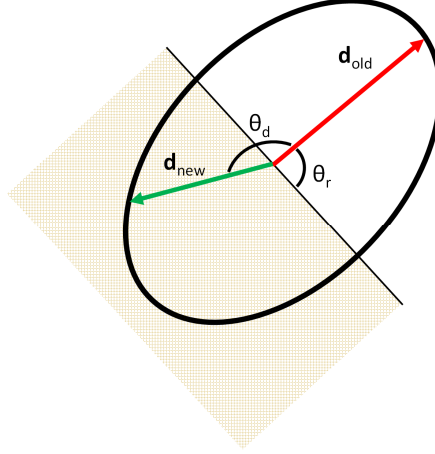
Figure 17: Reverse loading criterion for the proposed constitutive model.

Hence, for reverse loading to occur $\theta_d \geq \theta_r$, where

$$\theta_d = cos^{-1}\left(\frac{\boldsymbol{\sigma}_{(n)}}{|\boldsymbol{\sigma}_{(n)}|} : \frac{\boldsymbol{\sigma}_{(n+1)}}{|\boldsymbol{\sigma}_{(n+1)}|}\right) = cos^{-1}(\boldsymbol{d}_{old} \cdot \boldsymbol{d}_{new}) \tag{4}$$

where $\boldsymbol{\sigma}_{(n)}$ and $\boldsymbol{\sigma}_{(n+1)}$ are the stress tensors for the previous and the current time steps respectively.

In the current work, three separate yield surfaces are employed to model the yielding behavior within each deformation mode (i.e. ML, RC and RT). This multi-yield surface approach is rather similar to the one employed by Nguyen et al. [2013], where multiple isotropic Von Mises yield surfaces were used to model the hardening behavior within different deformation modes (i.e. slip,

twinning, untwinning). However, in the present work, a separate anisotropic CPB06 type yield surface (Cazacu et al. [2006]) is used to capture the evolving asymmetric/anisotropic hardening response within each deformation mode. Hence, a total of three CPB06 type yield surfaces are used and at any instant during the deformation process, only the yield surface corresponding to the current deformation mode stays active. The yield surface for each deformation mode (i.e. ML, RC or RT) evolves following the reference hardening equation and a set of evolving anisotropy parameters corresponding to that particular deformation mode. Furthermore, the initial size of the activated yield surface is determined by the amount of plastic prestrain accumulated during the previous deformation mode.

It is noted that, the current model is phenomenological and does not essentially represent the cyclic hardening behavior of magnesium alloys from a microstructure or deformation mechanics perspective. However, the macroscopic effects of these different deformation mechanisms and textural evolution on cyclic hardening and plastic anisotropy, are taken into account in the development of the proposed model.

6.2   Hardening evolution models

The strain hardening models proposed in this section are used to represent the isotropic expansion of the activated yield surface with accumulated plastic strain. For this purpose, a reference flow stress equation is defined for each of the three deformation modes. The initial size of the activated yield surface is influenced by the level of plastic prestrain during the previous deformation mode and its expansion is controlled by the local accumulated plastic strain within the active deformation mode

6.2.1   Monotonic Loading (ML) mode

ML (MODE 1) is the default deformation mode and is automatically activated at the beginning of the deformation process. Initial plastic deformation from the undeformed state (i.e. plastic prestrain = 0) always takes place within this mode until the loading is reversed. The true stress – true plastic strain curve for uniaxial tension along RD is chosen as the reference flow curve for representing

the isotropic hardening behavior during this deformation mode. The isotropic hardening response for ML mode $\tilde{\sigma}_{ML}^{iso}(\bar{\varepsilon}_{ML}^{p})$ is fitted using a modified Hockett-Sherby type hardening law as follows

$$\tilde{\sigma}_{ML}^{iso}(\bar{\varepsilon}_{ML}^{p}) = \sigma_{0,ML} + A_{ML}\left(1 - \exp\left(-C_{ML}\,\bar{\varepsilon}_{ML}^{p}\,^{B_{ML}}\right)\right) \tag{5}$$

where $\sigma_{0,ML}, A_{ML}, B_{ML}, C_{ML}$ are material parameters for the reference hardening curve representing uniaxial tension along RD and $\bar{\varepsilon}_{ML}^{p}$ is the corresponding local accumulated plastic strain for ML mode.

6.2.2 Reverse Compression (RC) mode

The isotropic hardening response for RC mode is obtained from the reverse compression portion of the cyclic curves. At a given plastic prestrain level, the reverse compression curve along RD is used as the reference flow curve and the isotropic hardening response $\tilde{\sigma}_{RC}^{iso}(\bar{\varepsilon}_{RC}^{p})$ is modelled using a Boltzmann type hardening law given below

$$\tilde{\sigma}_{RC}^{iso}(\bar{\varepsilon}_{RC}^{p}) = \sigma_{0,RC} + \frac{\sigma_{max,RC} - \sigma_{0,RC}}{1 + \exp(-(\bar{\varepsilon}_{RC}^{p} - \varepsilon_{0,RC})/\delta\varepsilon_{RC})} \tag{6}$$

where $\sigma_{0,RC}, \sigma_{max,RC}, \varepsilon_{0,RC}, \delta\varepsilon_{RC}$ are material parameters and $\bar{\varepsilon}_{RC}^{p}$ is the local accumulated plastic strain for RC mode. The material parameter $\sigma_{max,RC}$ is related to the upper stress plateau of the compressive sigmoidal flow curve, $\varepsilon_{0,RC}$ controls the transition from the twin-dominated flow regime to the slip-dominated flow regime (i.e. point of inflection), and $\delta\varepsilon_{RC}$ controls the width and steepness of this transition region. As observed in Section 5.6 previously, an increase in tensile prestrain leads to an increase in the reverse compressive yield stress and the hardening rate when the loading is reversed. To account for this hardening effect, the parameters in Eq. (6) are expressed as function of tensile plastic prestrain $\bar{\varepsilon}_{T}^{p*}$, which is identified by the accumulated plastic strain during the previous deformation mode.

6.2.3 Reverse Tension (RT) mode

The reverse tension portion of the cyclic hardening curves are used to represent the isotropic hardening response for RT mode. The hardening behavior for reverse tension following previous compression is comparatively complex and cannot be captured accurately using a single

Boltzmann type sigmoid function. This is partly due to the occurrence of a Bauschinger-type non-linear unloading curve and due to the absence of an abrupt elastic-to-plastic transition region upon reverse tensile loading (see Figure 14 and Figure 15). Furthermore, the exhaustion of untwinning upon reverse tension leads to the initiation of a slip dominated deformation with an exponentially decaying hardening rate. It is noted that for the case of reverse compression, the experimental compressive strains are not high enough to cause exhaustion of twinning dominant deformation. Therefore, the use of a single sigmoid function was deemed sufficient to capture the hardening response during reverse compression. For the current case of reverse tension, a new modified Voce-Boltzmann type hardening law is used to represent the hardening response for improved accuracy. The proposed isotropic hardening law for RT mode is written as follows

$$
\begin{aligned}
\tilde{\sigma}_{RT}^{iso}\left(\bar{\varepsilon}_{RT}^{p}\right) = \sigma_{0,RT} &+ \sigma_{1,RT}\left[\left(1 - \exp\left(-C_{1,RT}\ \bar{\varepsilon}_{RT}^{p}\right)\right) + \frac{3}{4}\left(1 - \exp\left(-C_{2,RT}\ \bar{\varepsilon}_{RT}^{p}\ ^{B_{RT}}\right)\right)\right] \\
&+ \frac{\sigma_{max,RT}\ -\ \sigma_{0,RT}\ -\ \dfrac{7}{4}\left(\sigma_{1,RT}\right)}{1 + \exp\left(-\left(\bar{\varepsilon}_{RT}^{p} - \varepsilon_{0,RT}\right)/\delta\varepsilon_{RT}\right)}
\end{aligned}
\tag{7}
$$

where $\sigma_{0,RT}$, $\sigma_{1,RT}$, $\sigma_{max,RT}$, B_{RT}, $C_{1,RT}$, $C_{2,RT}$, $\varepsilon_{0,RT}$, $\delta\varepsilon_{RT}$ are material parameters and $\bar{\varepsilon}_{RT}^{p}$ is the local accumulated plastic strain for RT mode. The material parameter $\sigma_{1,RT}$ in Eq. (7) is associated with the lower flow stress plateau of the reverse tension sigmoidal curve (i.e. region with relatively lower hardening rate due to untwinning dominant deformation), $\sigma_{max,RT}$ is linked with the upper stress plateau of the reverse tension sigmoidal curve, $\varepsilon_{0,RT}$ controls the transition from the untwinning dominant flow regime to the slip dominant flow regime (i.e. point of inflection) and $\delta\varepsilon_{RT}$ controls the steepness of this transition region. In general, the 2nd term on the left hand side in Eq. (7) accounts for the initial low hardening rate experienced during untwinning dominant deformation whereas the last term accounts for the change in hardening behavior due to the transition from untwinning-to-slip dominated deformation. The 3rd term, in between the previous two, is used to improve the overall smoothness and accuracy of the modelled hardening response to the experimental data. Furthermore, in order to account for the effects of compressive prestrain on reverse tensile yield stress and subsequent hardening behavior during reverse tension, the material parameters in Eq. (7) are expressed as a function of compressive plastic prestrain $\bar{\varepsilon}_{C}^{p*}$ accumulated during the previous deformation mode.

6.2.4   Identification of hardening parameters and application to ZEK100 and AZ31B

The flow stress curves for monotonic tension in RD (Section 5.2) and cyclic CTC and TCT curves in RD (Section 5.6) for ZEK100 and AZ31B sheet alloys are used to obtain the material parameters associated with the hardening models developed in the previous section. The material parameters are obtained by fitting the hardening models to the corresponding experimental data for each deformation mode using non-linear least square regression based on the Trust-Region algorithm available within Matlab®.

The stress strain curve for uniaxial tension along RD was used to obtain the material parameters associated with the isotropic hardening response for ML mode $\widetilde{\sigma}_{ML}^{iso}\left(\bar{\varepsilon}_{ML}^{p}\right)$. It is noted that, the material parameters for isotropic hardening response in ML mode could also be obtained by using the initial tension portion of cyclic TCT curve along RD but the stress-strain curve for uniaxial tension along RD is used instead as it can capture the experimental hardening response for a much larger strain range which is not achieved during initial tension portion of cyclic TCT tests. However, before proceeding, it is ascertained that the experimental stress-strain curve for uniaxial tension along RD is indeed identical to the initial tension portion of cyclic TCT curve along RD. The material parameters used in Eq. (5) for ML mode are given in Table 4.

Table 4: Material parameters for the isotropic hardening model of ML mode.

Material	$\sigma_{0,ML}$ (MPa)	A_{ML} (MPa)	B_{ML}	C_{ML}
AZ31B	161	173.3591	0.9503	10.6638
ZEK100	129	142.3007	0.2783	9.27440

For fitting the hardening response during RC and RT mode, the cyclic CTC and TCT curves for ZEK100 and AZ31B sheet alloys are each partitioned into three segments based on the type of loading (i.e. initial compression or initial tension, reverse compression, reverse tension). Next, the flow stress segments for reverse compression and reverse tension were used to establish stress-strain relationships for reverse compression and reverse tension with respect to the corresponding local plastic strains $\bar{\varepsilon}_{RC}^{p}$ and $\bar{\varepsilon}_{RT}^{p}$ respectively. These modified stress-strain curves are then used to obtain the material parameters associated with the hardening response for RC mode $\widetilde{\sigma}_{RC}^{iso}\left(\bar{\varepsilon}_{RC}^{p}\right)$ (Table 5) and RT mode $\widetilde{\sigma}_{RT}^{iso}\left(\bar{\varepsilon}_{RT}^{p}\right)$ (Table 6) respectively.

Table 5: Material parameters for the isotropic hardening model of RC mode

Material	Test Type	$\bar{\varepsilon}_T^{p*}$ (Prestrain)	$\sigma_{0,RC}$ (MPa)	$\sigma_{max,RC}$ (MPa)	$\varepsilon_{0,RC}$	$\delta\varepsilon_{RC}$
AZ31B	CTC	1) 0.0304	94.9255	460.000	0.0827	0.0239
		2) 0.0671	124.868	485.000	0.0838	0.0205
		3) 0.1055	155.000	503.555	0.0801	0.0167
	TCT	4) 0.0154	97.6402	413.912	0.0770	0.0213
		5) 0.0340	120.000	449.058	0.0808	0.0172
		6) 0.0526	134.258	464.252	0.0817	0.0152
ZEK100	CTC	1) 0.0301	91.6155	393.000	0.0807	0.0251
		2) 0.0676	117.910	405.251	0.0870	0.0223
		3) 0.1065	142.581	422.000	0.0885	0.0217
	TCT	4) 0.0158	42.9361	375.000	0.0950	0.0540
		5) 0.0346	96.6728	385.000	0.0908	0.0280
		6) 0.0534	117.624	400.000	0.0922	0.0215

Table 6: Material parameters for the isotropic hardening model of RT mode

Material	Cyclic Test	$\bar{\varepsilon}_C^{p*}$ (Prestrain)	$\sigma_{0,RT}$ (MPa)	$\sigma_{1,RT}$ (MPa)	$\sigma_{max,RT}$ (MPa)	B_{RT}	$C_{1,RT}$	$C_{2,RT}$	$\varepsilon_{0,RT}$	$\delta\varepsilon_{RT}$
AZ31B	CTC	1) 0.0173	22.394	58.000	230.233	3.494	230.900	294203	0.016	0.001
		2) 0.0379	31.665	63.000	280.947	3.831	133.150	62168.1	0.034	0.003
		3) 0.0580	43.935	68.000	323.935	2.648	145.916	799.170	0.053	0.004
	TCT	4) 0.0283	28.845	100.00	327.845	1.905	79.2850	96.0130	0.026	0.002
		5) 0.0655	45.539	75.000	337.789	1.920	297.319	269.868	0.059	0.004
		6) 0.1020	103.72	54.000	375.215	2.144	558.786	840.531	0.073	0.009
ZEK100	CTC	1) 0.0179	21.432	64.000	201.182	2.365	146.436	7225.69	0.015	0.001
		2) 0.0380	30.252	66.500	240.777	2.726	140.172	2332.24	0.033	0.003
		3) 0.0580	41.329	69.000	259.579	2.413	153.485	645.960	0.052	0.006
	TCT	4) 0.0290	26.788	68.000	260.757	1.925	170.984	184.336	0.025	0.003
		5) 0.0670	43.023	70.000	273.217	1.840	216.947	255.533	0.058	0.006
		6) 0.1040	68.718	72.500	306.834	2.247	258.118	420.754	0.080	0.012

In Table 5, for a given material, the first three tensile prestrain $\bar{\varepsilon}_T^{p*}$ values correspond to reverse compression during CTC tests and the next three tensile prestrain $\bar{\varepsilon}_T^{p*}$ values correspond to reverse compression during TCT tests. Similarly, in Table 6, the first three compressive prestrain $\bar{\varepsilon}_C^{p*}$ values correspond to reverse tension during CTC tests and the next three compressive prestrain $\bar{\varepsilon}_C^{p*}$ values correspond to reverse tension during TCT tests. It is noted that, the material parameters given in Table 5 and Table 6 are not constants and vary with the amount of plastic prestrain accumulated during the previous deformation mode. For general loading cases where the prestrain upon reverse loading is different than experimentally obtained values, the material parameters are interpolated from those listed. A similar approach was previously used by Nguyen et al. [2013], for modelling reverse hardening behavior in AZ31 sheets.

6.3   Anisotropic yield criteria

6.3.1   Yield criterion background

Cazacu et al. [2006] proposed an isotopic pressure-insensitive yield criterion to account for the tension-compression yielding asymmetry associated with deformation twinning in HCP metals. The yield criterion is defined as

$$F(\mathbf{S}) = (|S_1| - kS_1)^a + (|S_2| - kS_2)^a + (|S_3| - kS_3)^a \tag{8}$$

where $S_i, i = 1, \ldots, 3$, are the principal values of $\mathbf{S}$ which is the deviator of the Cauchy stress $\boldsymbol{\sigma}$, the integer a is the degree of homogeneity and the coefficient k represents the strength differential effect between tension and compression. The isotropic yield criterion (Eq. (8)) was further extended to orthotropy by applying a linear transformation on the deviatoric stress tensor $\mathbf{S}$. The resulting anisotropic yield criterion CPB06 is written as

$$F(\boldsymbol{\Sigma}) = (|\Sigma_1| - k\Sigma_1)^a + (|\Sigma_2| - k\Sigma_2)^a + (|\Sigma_3| - k\Sigma_3)^a \tag{9}$$

where $\Sigma_1, \Sigma_2, \Sigma_3$ are the principal values of the transformed stress tensor $\boldsymbol{\Sigma}$. The transformed stress tensor $\boldsymbol{\Sigma}$ is defined as

$$\boldsymbol{\Sigma} = \mathbf{C} : \mathbf{S} \tag{10}$$

where $\mathbf{C}$ is a fourth-order symmetric tensor that describes material's anisotropy and $\mathbf{S}$ is the deviatoric stress tensor. With respect to the (x, y, z) coordinate system (where $x, y \ and \ z$ represent the sheet RD, TD and ND, respectively) the orthotropic tensor $\mathbf{C}$ is represented as

$$\mathbf{C} = \begin{bmatrix} C_{11} & C_{12} & C_{13} & 0 & 0 & 0 \\ C_{12} & C_{22} & C_{23} & 0 & 0 & 0 \\ C_{13} & C_{23} & C_{33} & 0 & 0 & 0 \\ 0 & 0 & 0 & C_{44} & 0 & 0 \\ 0 & 0 & 0 & 0 & C_{55} & 0 \\ 0 & 0 & 0 & 0 & 0 & C_{66} \end{bmatrix} \tag{11}$$

The CPB06 yield criterion (Eq. (9)) is insensitive to hydrostatic pressure; thus, the condition for plastic incompressibility is satisfied. Also, for $k \in [-1,1]$ and any integer $a \geq 1$, the anisotropic yield function is convex in the variables $\Sigma_1, \Sigma_2, \Sigma_3$ (see Cazacu et al. [2004]).

Plunkett et al. [2008] demonstrated that additional linear transformations can be incorporated into CPB06 to improve the representation of the anisotropic yield surface. Recently, Ghaffari Tari et al. [2013] successfully employed three linear transformations of the stress deviator to capture the hardening behavior of AZ31B magnesium alloy under monotonic loading conditions. However, in the current modeling approach, two linear stress transformations are deemed sufficient to represent the anisotropic behavior of both AZ31B and ZEK100 magnesium alloys. The yield criterion with two stress transformations (CPB06ex2) can be written as:

$$
\begin{aligned}
F(\boldsymbol{\Sigma}, \boldsymbol{\Sigma'}) = &(|\Sigma_1| - k\Sigma_1)^a + (|\Sigma_2| - k\Sigma_2)^a + (|\Sigma_3| - k\Sigma_3)^a + (|\Sigma_1'| - k'\Sigma_1')^a \\
&+ (|\Sigma_2'| - k'\Sigma_2')^a + (|\Sigma_3'| - k'\Sigma_3')^a
\end{aligned}
\tag{12}
$$

where k and k' are the strength differential parameters and the new tensor $\boldsymbol{\Sigma'}$ is given by:

$$
\boldsymbol{\Sigma'} = \mathbf{C'} : \mathbf{S}
\tag{13}
$$

where the fourth-order orthotropic tensor $\mathbf{C'}$ has a similar representation to that of tensor $\mathbf{C}$ given in Eq. (11). For a 3D stress state and orthotropic symmetry, the tensors $\mathbf{C}$ and $\mathbf{C'}$, have nine non-zero components each. However, for the plane stress formulation implied in this work, $\mathbf{C}$ and $\mathbf{C'}$, have seven non-zero components since the parameters $C_{44} = C_{55} = C'_{44} = C'_{55} = 0$. It is noted that, when $\mathbf{C} = \mathbf{C'}$, and $k = k'$, the CPB06ex2 yield criterion (Eq. (12)) reduces to the original anisotropic yield criterion CPB06 (Eq. (9)).

6.3.2   Yield criterion extension to include evolving anisotropy/asymmetry

Deformation twinning inevitably leads to texture evolution in HCP metals such as magnesium alloys. On a macroscopic scale, texture evolution leads to an evolving plastic anisotropy and tension-compression flow stress asymmetry as shown by the experimental results presented in the earlier sections of this paper. The CPB06 yield criterion presented in the previous section is able to represent individual plane stress yield loci for given fixed levels of accumulated plastic deformation as shown by Cazacu et al., [2006] and Plunkett et al. [2008]. However, in order to account for the continuous evolution of plastic anisotropy and tension-compression asymmetry, the shape of the yield locus should also change with the accumulated plastic deformation. Accordingly, this means that the anisotropy coefficients and strength differential parameters

involved in the expression of CPB06ex2 yield criterion (Eq. 12) must also evolve with accumulated plastic deformation. Thus, it is assumed that yielding condition has the following general form

$$F(\boldsymbol{\sigma}, \bar{\varepsilon}^p) = \bar{\sigma}\big(\boldsymbol{\sigma}, \boldsymbol{C}(\bar{\varepsilon}^p), \boldsymbol{C}'(\bar{\varepsilon}^p), k(\bar{\varepsilon}^p), k'(\bar{\varepsilon}^p)\big) - \tilde{\sigma}^{iso}(\bar{\varepsilon}^p) \qquad (14)$$

where $\bar{\sigma}$ is the effective stress based on the CPB06ex2 stress potential given in Eq. (12), $\tilde{\sigma}^{iso}(\bar{\varepsilon}^p)$ is the isotropic hardening law and $\bar{\varepsilon}^p$ is the effective plastic strain associated with the anisotropic yield function using the work-equivalence principle (Hill [1987]). In the current work, each of the three deformation modes (i.e. ML, RC, and RT) has been assigned a CPB06ex2 yield surface and at any instant in time, only one of the three yield surfaces corresponding to the current deformation mode is active. Furthermore, the anisotropy coefficients and strength differential parameters are considered to be evolving with the local accumulated plastic deformation within each mode. The modified yielding condition for each deformation mode is of the following form

$$F(\boldsymbol{\sigma}, \bar{\varepsilon}^p) = \begin{cases} \bar{\sigma}_{ML}\left(\boldsymbol{\sigma}, \boldsymbol{C}(\bar{\varepsilon}^p_{ML}), \boldsymbol{C}'(\bar{\varepsilon}^p_{ML}), k(\bar{\varepsilon}^p_{ML}), k'(\bar{\varepsilon}^p_{ML})\right) - \tilde{\sigma}^{iso}_{ML}(\bar{\varepsilon}^p_{ML}) \ for \ ML \ (MODE \ 1) \\ \bar{\sigma}_{RC}\left(\boldsymbol{\sigma}, \boldsymbol{C}(\bar{\varepsilon}^p_{RC}), \boldsymbol{C}'(\bar{\varepsilon}^p_{RC}), k(\bar{\varepsilon}^p_{RC}), k'(\bar{\varepsilon}^p_{RC})\right) - \tilde{\sigma}^{iso}_{RC}(\bar{\varepsilon}^p_{RC}) \ for \ RC \ (MODE \ 2) \\ \bar{\sigma}_{RT}\left(\boldsymbol{\sigma}, \boldsymbol{C}(\bar{\varepsilon}^p_{RT}), \boldsymbol{C}'(\bar{\varepsilon}^p_{RT}), k(\bar{\varepsilon}^p_{RT}), k'(\bar{\varepsilon}^p_{RT})\right) - \tilde{\sigma}^{iso}_{RT}(\bar{\varepsilon}^p_{RT}) \ for \ RT \ (MODE \ 3) \end{cases} \qquad (15)$$

where $\bar{\sigma}_{ML}, \bar{\sigma}_{RC}, \bar{\sigma}_{RT}$ are the effective stresses and $\tilde{\sigma}^{iso}_{ML}(\bar{\varepsilon}^p_{ML}), \tilde{\sigma}^{iso}_{RC}(\bar{\varepsilon}^p_{RC}), \tilde{\sigma}^{iso}_{RT}(\bar{\varepsilon}^p_{RT})$ represent the isotropic hardening laws corresponding to ML, RC and RT deformation modes, respectively.

Several approaches has been implemented, where saturating exponential functions (Steglich et al. [2011], Ghaffari Tari et al. [2013]) or sine damping functions (Yoon et al. [2013]) are used to capture the variation of anisotropy coefficients and strength differential parameters with accumulated plastic deformation for monotonic loading conditions. An alternative approach, proposed by Plunkett et al. [2006], consists of determining the anisotropy coefficients corresponding to several fixed levels of accumulated plastic deformation. Afterwards, a piece-wise linear interpolation is used to obtain the yield surface corresponding to any level of accumulated plastic deformation.

In the present work, the methodology proposed by Plunkett et al. [2006] in conjunction with the anisotropic CPB06ex2 yield criterion has been used. For each deformation mode, the

anisotropic/asymmetric evolution of its associated yield locus is captured by calculating the anisotropy (i.e. C_{ij} and C'_{ij}) and strength differential parameters (i.e. k and k') for m fixed levels of the local effective plastic strains $\bar{\varepsilon}^{p,(1)} < \bar{\varepsilon}^{p,(2)} < \cdots < \bar{\varepsilon}^{p,(m)}$. Next, for each deformation mode, the effective stress corresponding to each individual effective plastic strain level $\bar{\varepsilon}^{p,(j)}$, $j = 1, \ldots, m$ is calculated using $\bar{\sigma}^{(j)} = \bar{\sigma}\left(\boldsymbol{\sigma}, \boldsymbol{C}\left(\bar{\varepsilon}^{p,(j)}\right), \boldsymbol{C}'\left(\bar{\varepsilon}^{p,(j)}\right), k\left(\bar{\varepsilon}^{p,(j)}\right), k'\left(\bar{\varepsilon}^{p,(j)}\right)\right)$ according to Eq. (15). The effective stress corresponding to any intermediate level of accumulated plastic strain $\left(\bar{\varepsilon}^{p,(j)} \leq \bar{\varepsilon}^p \leq \bar{\varepsilon}^{p,(j+1)}, j = 1, \ldots, m-1\right)$ is determined using linear interpolation as follows

$$\bar{\sigma} = \psi(\bar{\varepsilon}^p).\bar{\sigma}^{(j)} + \left(1 - \psi(\bar{\varepsilon}^p)\right).\bar{\sigma}^{(j+1)} \tag{16}$$

where $\psi(\bar{\varepsilon}^p)$ is an interpolation weighting factor and it is defined as

$$\psi(\bar{\varepsilon}^p) = \frac{\bar{\varepsilon}^{p,(j+1)} - \bar{\varepsilon}^p}{\bar{\varepsilon}^{p,(j+1)} - \bar{\varepsilon}^{p,(j)}} \tag{17}$$

such that $\psi\left(\bar{\varepsilon}_p^{(j)}\right) = 1$ and $\psi\left(\bar{\varepsilon}_p^{(j+1)}\right) = 0$.

6.3.3 Yield surface calibration and application to ZEK100 and AZ31B

6.3.3.1 General calibration approach

For each deformation mode, the anisotropy (i.e. C_{ij} and C'_{ij}) and strength differential parameters (i.e. k and k') involved in Eq. (15) are determined by minimizing the difference between the corresponding stress potential function and the experimental data. The error minimization approach due to Plunkett et al. [2008] has been adopted in this work. The experimental data used in the calibration process includes the flow stresses and the r-values in tension and compression corresponding to the three in-plane sheet orientations (i.e. RD, DD and TD) as well as the in-plane biaxial flow stresses in tension and compression. The yield surface anisotropy parameters are found by minimizing the following error function

$$E(C, C', k, k') = \sum_i w_i \left(\frac{\sigma_i^{th}}{\sigma_i^{exp}} - 1\right)^2 + \sum_j w_j \left(\frac{r_j^{th}}{r_j^{exp}} - 1\right)^2 \tag{18}$$

In the above equation, σ_i^{th} and r_j^{th} represent the yield function response for flow stresses and r-values respectively, while σ_i^{exp} and r_j^{exp} are the associated experimental values. The subscript i and j represent the number of experimental flow stresses and r-values, respectively, used in the calibration process and w represents the corresponding weighing factors given to the experimental data. In the present work, the degree of homogeneity a in Eq. (12) is set to $a = 6$, based on previous modeling work of Ghaffari Tari et al. [2013]. For the exact relations used for σ_i^{th} and r_j^{th} in Eq. (18), readers are referred to see Appendix A. The non-linear minimization of the error function is performed using the commercial software Matlab®. The minimization process is repeated several times while adjusting the weighing factors and initial guesses until satisfactory results are achieved.

In the present work, for each deformation mode, the corresponding anisotropy (i.e. C_{ij} and C'_{ij}) and strength differential parameters (i.e. k and k') are calculated for hundred fixed levels (i.e. $m = 100$) of the local accumulated plastic strains starting with $\bar{\varepsilon}^p = 0\%$ and ending at $\bar{\varepsilon}^p = 10\%$ with an increment of $\Delta\bar{\varepsilon}^p = 0.1\%$.

6.3.3.2 Calibration for ML (MODE 1)

The experimental flow stresses for monotonic loading given in Section 5.2 and the experimental r-values given in Section 5.4 are used for calibrating the yield surface corresponding to the ML mode. At a given level of local effective plastic strain, a total of 14 experimental values are used for calibration including: three flow stresses and instantaneous r-values for tensile loading along RD, DD and TD, three flow stresses and instantaneous r-values for compressive loading along RD, DD and TD, the equi-biaxial tension, and the equi-biaxial compression flow stresses. Using the assumption of plastic incompressibility, the experimental flow stress for ND (through-thickness) compression is used to represent the yielding behavior in equi-biaxial tension. The experimental data for equi-biaxial compression is not available at the present time. However, in order to control the yielding response in that regime, the equi-biaxial compression flow stress is assumed to be equal to the average of RD and TD flow stresses in compression. Similar assumptions were used

by Ghaffari Tari et al. [2013] to represent the behavior of AZ31B sheet in equi-biaxial tension and compression regimes.

Figure 18 shows the evolution of anisotropy/asymmetry parameters with local effective plastic strain $\bar{\varepsilon}_{ML}^{p}$ (i.e. $\bar{\varepsilon}_{ML}^{p}$ = 0, 0.001, 0.002, ..., 0.099, 0.1) for ZEK100 and AZ31B alloys. It is observed that the anisotropy parameters evolve rapidly with accumulated plastic strain and tend to reach an almost constant value with continuing plastic deformation. This is rather expected because of the exhaustion of deformation twinning which is the major cause of texture evolution and anisotropy in Mg alloys.
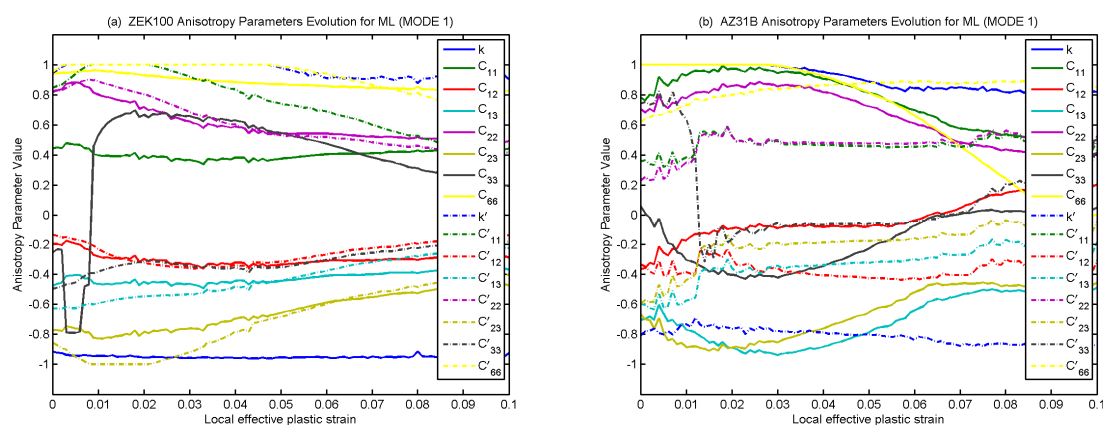
Figure 18: Evolution of anisotropy coefficients and strength differential parameters for (a) ZEK100 (b) AZ31B corresponding to ML mode (MODE 1)

6.3.3.3 Calibration for RC (MODE 2) and RT (MODE 3)

The experimental CTC and TCT flow stresses given in Section 5.6 are used for calibrating the yield surfaces corresponding to RC and RT deformation modes. Since the loading during RC deformation mode is always compressive, the yield surfaces for RC mode are calibrated for compression regime (i.e. $\Delta\varepsilon_1 + \Delta\varepsilon_2 < 0$) and similarly the yield surfaces corresponding to RT mode are only calibrated within the tension regime (i.e. $\Delta\varepsilon_1 + \Delta\varepsilon_2 \geq 0$). To simplify the calibration process, the strength differential parameters associated with the respective yield functions for RC and RT mode are set equal to zero (i.e. $k = k' = 0$) as we are dealing with compressive-only or tensile-only loading during RC and RT modes respectively. At a given level of local effective plastic strain (i.e. $\bar{\varepsilon}_{RC}^{p}$, $\bar{\varepsilon}_{RT}^{p}$ for RC and RT modes respectively), a total of 7

experimental values are used in calibration process. For calibration of RC mode, the values include the three flow stresses and instantaneous r-values for reverse compression along RD, DD, TD and the equi-biaxial compression flow stress. Similarly, for calibration of RT mode, the experimental values include the three flow stresses and instantaneous r-values for reverse tension along RD, DD, TD and the equi-biaxial tension flow stress. The experimental results for the evolution of r-values during reverse compression and reverse tension along RD, DD, and TD are not available at the present time. However, in order to constrain the slope of yield locus at these locations, the values are assumed to be constant and are set equal to the corresponding r-values for monotonic loading tests at an accumulated plastic strain of 0.1. Furthermore, for AZ31B sheet material, the experimental CTC and TCT tests were only conducted in RD and hence the results for DD and TD test directions are not available. However, as mentioned previously, with the exception of differences in experimental yield stresses among the three test directions, the hardening behavior observed during CTC and TCT tests of AZ31B is similar (Lou et al. [2007]). Therefore, it is assumed that the CTC and TCT flow curves for DD and TD test directions of AZ31B can be represented by multiplying (i.e. scaling) the CTC and TCT flow curves in RD by the corresponding yield stress anisotropy ratios (i.e. σ_{DD}/σ_{RD}, σ_{TD}/σ_{RD}) observed in monotonic tension tests.

The anisotropy parameters for RC and RT deformation modes are calculated for each of the six corresponding experimentally tested prestrain conditions listed in Table 5 and Table 6. For general loading conditions where the prestrain is different from those listed, the anisotropy parameters corresponding to the closest tested prestrain are used. Figure 19 shows the evolution of anisotropy parameters corresponding to prestrain 1 (see Table 5 and Table 6) for RC and RT deformation modes of ZEK100 and AZ31B sheets. Similar evolutionary relationships are established for the remaining five experimental prestrain conditions. However, for simplicity they are not shown here.

42
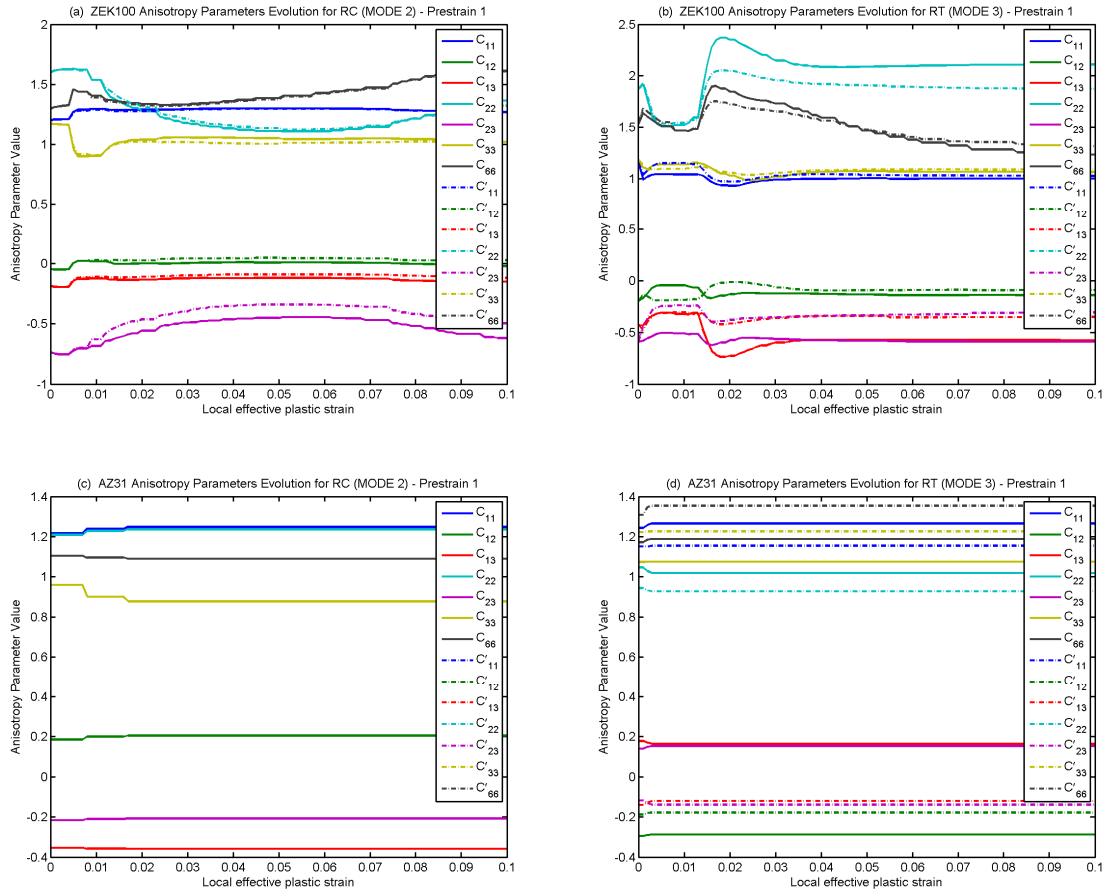
Figure 19: Evolution of anisotropy coefficients for (a) ZEK100 – RC deformation mode (b) ZEK100 – RT deformation mode (c) AZ31B – RC deformation mode (d) AZ31B – RT deformation mode

The anisotropy parameters for RC and RT modes of AZ31B (Figure 19 (c-d)) are almost constant and do not change with the corresponding local effective plastic strains. This is consistent with the calibration approach explained in this section for RC and RT deformation modes of AZ31B.

Chapter 7: Numerical Implementation

The proposed constitutive model was implemented as a user material subroutine (UMAT) in the commercially available software LS-DYNA within the framework of rate independent plasticity. In the present work, the incremental theory of plasticity (Chung and Richmond [1993], Yoon et al. [1999]) was applied to the elasto-plastic formulation based on the materially embedded coordinate system; thus, ensuring the objectivity of the Cauchy stress tensor. Since elastic strains are usually much smaller than plastic strains, an additive decomposition of the total strain rate $\dot{\boldsymbol{\varepsilon}}$ into an elastic part $\dot{\boldsymbol{\varepsilon}}^e$ and a plastic part $\dot{\boldsymbol{\varepsilon}}^p$ is considered as follows

$$\dot{\boldsymbol{\varepsilon}} = \dot{\boldsymbol{\varepsilon}}^e + \dot{\boldsymbol{\varepsilon}}^p \tag{19}$$

The elastic stress strain relationship is given by

$$\dot{\boldsymbol{\sigma}} = \boldsymbol{C}^e : \dot{\boldsymbol{\varepsilon}}^e \tag{20}$$

where $\boldsymbol{C}^e$ is the fourth-order elasticity tensor. The incremental plastic strain is determined by an associated flow rule given below

$$\dot{\boldsymbol{\varepsilon}}^p = \dot{\lambda}\frac{\partial F}{\partial \boldsymbol{\sigma}} \tag{21}$$

where F is the yield function defined by Eq. (4414) and $\dot{\lambda}$ is the plastic multiplier. The loading-unloading conditions are expressed in the standard Karush-Khun-Tucker form (Simo and Hughes [1998]) as follows

$$\dot{\lambda} \geq 0, \quad F \leq 0, \quad \dot{\lambda}F = 0 \tag{22}$$

Furthermore, as the effective stress $\bar{\sigma}$ is a first order homogeneous function in stresses, it then follows from the work-equivalence principle that $\dot{\lambda} = \Delta\bar{\varepsilon}^p$ where $\Delta\bar{\varepsilon}^p$ is the effective plastic strain increment.

In the present work, the stress integration framework based on the cutting-plane return mapping algorithm proposed by Simo and Ortiz [1985], Ortiz and Simo [1986] is adopted for integration of the elasto-plastic constitutive relations. A similar stress integration approach was previously used by Abedrabbo et al. [2006,2007] for implementing a UMAT into the explicit LS-DYNA code for conducting warm forming simulations of aluminum alloys using YLD96 (Barlat et al. [1997]) and

YLD2000-2d (Barlat et al. [2003]) type yield functions. Using the proposed approach, at the beginning of each time step t, a trial stress state σ_{n+1}^{trial} is calculated by assuming a pure elastic deformation as follows

$$\sigma_{(n+1)}^{trial} = \sigma_{(n)} + C^e : \dot{\varepsilon}_{(n+1)} \tag{23}$$

where $\sigma_{(n)}$ is the stress state at the end of nth (previous) time increment and $\dot{\varepsilon}_{(n+1)}$ is the current strain increment. Next based on the current active deformation mode, the following procedure is followed.

7.1 Monotonic Loading (ML) mode

Using the calculated trial stress state $\sigma_{(n+1)}^{trial}$, the yielding condition for ML deformation mode is defined as

$$F_{ML}\left(\sigma_{(n+1)}^{trial}, \bar{\varepsilon}_{ML,(n)}^p\right) = \bar{\sigma}_{ML}\left(\sigma_{(n+1)}^{trial}, \bar{\varepsilon}_{ML,(n)}^p\right) - \tilde{\sigma}_{ML}^{iso}\left(\bar{\varepsilon}_{ML,(n)}^p\right) \leq 0 \tag{24}$$

If the above condition is satisfied, then the trial stress state is elastic and the calculated trial stress is the actual stress state (i.e. $\sigma_{n+1} = \sigma_{n+1}^{trial}$) for that time increment. However, if the condition is not satisfied then there is plastic flow and the Newton-Raphson method is used to iteratively return the trial stress state to the yield surface. This is done by calculating the normality parameter $\dot{\lambda}$ at the beginning of each kth iteration and sequentially updating the stress state and the effective plastic strain as follows

$$\begin{cases} \sigma_{(n+1)}^{(k+1)} = \sigma_{(n+1)}^{(k)} - \dot{\lambda} \, C^e : \left(\frac{\partial F_{ML}}{\partial \sigma}\right)_{(n+1)}^{(k)} \\ \bar{\varepsilon}_{ML,(n+1)}^{p,(k+1)} = \bar{\varepsilon}_{ML,(n+1)}^{p,(k)} + \dot{\lambda} \end{cases} \tag{25}$$

where the term $-\dot{\lambda} \, C^e : \left(\frac{\partial F_{ML}}{\partial \sigma}\right)_{(n+1)}^{(k)}$ is the plastic corrector for return mapping of the stress state to the yield surface and k is the local iteration counter, with $k = 0$ representing the elastic trial stress state (i.e. $\sigma_{(n+1)}^{(k=0)} = \sigma_{(n+1)}^{trial}$ and $\bar{\varepsilon}_{ML,(n+1)}^{p,(k=0)} = \bar{\varepsilon}_{ML,(n)}^p$). Using the new stress state, the yielding check is performed once again as follows

$$F_{ML}\left(\boldsymbol{\sigma}_{(n+1)}^{(k+1)}, \bar{\varepsilon}_{ML,(n+1)}^{p,(k+1)}\right) = \bar{\sigma}_{ML}\left(\boldsymbol{\sigma}_{(n+1)}^{(k+1)}, \bar{\varepsilon}_{ML,(n+1)}^{p,(k+1)}\right) - \tilde{\sigma}_{ML}^{iso}\left(\bar{\varepsilon}_{ML,(n+1)}^{p,(k+1)}\right) \leq 0 \tag{26}$$

The plastic correction step is repeated for a number of iterations until the plastic consistency is restored within a set tolerance, i.e.

$$F_{ML}\left(\boldsymbol{\sigma}_{(n+1)}^{(k+1)}, \bar{\varepsilon}_{ML,(n+1)}^{p,(k+1)}\right) \leq \delta \tag{27}$$

where the residual parameter δ represents a small number, taken as 10^{-7} MPa in the current work. The relationship for the normality parameter $\dot{\lambda}$ is obtained through a Taylor expansion of the yield criterion as follows

$$
\begin{aligned}
0 = {}& F_{ML}\left(\boldsymbol{\sigma}_{(n+1)}^{(k)}, \bar{\varepsilon}_{ML,(n+1)}^{p,(k)}\right) + \left(\frac{\partial F_{ML}}{\partial \boldsymbol{\sigma}}\right)_{(n+1)}^{(k)}\left(\boldsymbol{\sigma}_{(n+1)}^{(k+1)} - \boldsymbol{\sigma}_{(n+1)}^{(k)}\right) \\
& + \left(\frac{\partial F_{ML}}{\partial \bar{\varepsilon}_{ML}^{p}}\right)_{(n+1)}^{(k)}\left(\bar{\varepsilon}_{ML,(n+1)}^{p,(k+1)} - \bar{\varepsilon}_{ML,(n+1)}^{p,(k)}\right)
\end{aligned}
\tag{28}
$$

Using Eq. (25), the above relationship can be rewritten as

$$
\begin{aligned}
0 = {}& F_{ML}\left(\boldsymbol{\sigma}_{(n+1)}^{(k)}, \bar{\varepsilon}_{ML,(n+1)}^{p,(k)}\right) + \left(\frac{\partial F_{ML}}{\partial \boldsymbol{\sigma}}\right)_{(n+1)}^{(k)}\left(-\dot{\lambda}\,\boldsymbol{C}^{e} : \left(\frac{\partial F_{ML}}{\partial \boldsymbol{\sigma}}\right)_{(n+1)}^{(k)}\right) \\
& + \dot{\lambda}\left(\frac{\partial F_{ML}}{\partial \bar{\varepsilon}_{ML}^{p}}\right)_{(n+1)}^{(k)}
\end{aligned}
\tag{29}
$$

Using Eq. (16-17), the derivatives in the previous equation are evaluated as follows

$$
\begin{cases}
\dfrac{\partial F_{ML}}{\partial \boldsymbol{\sigma}} = \dfrac{\partial \bar{\sigma}_{ML}}{\partial \boldsymbol{\sigma}} = \psi(\bar{\varepsilon}_{ML}^{p}) \cdot \dfrac{\partial \bar{\sigma}_{ML}^{(j)}}{\partial \boldsymbol{\sigma}} + \left(1 - \psi(\bar{\varepsilon}_{ML}^{p})\right) \cdot \dfrac{\partial \bar{\sigma}_{ML}^{(j+1)}}{\partial \boldsymbol{\sigma}} \\[2ex]
\dfrac{\partial F_{ML}}{\partial \bar{\varepsilon}_{ML}^{p}} = \dfrac{\partial \bar{\sigma}_{ML}}{\partial \bar{\varepsilon}_{ML}^{p}} - \dfrac{\partial \tilde{\sigma}_{ML}^{iso}}{\partial \bar{\varepsilon}_{ML}^{p}} \\[2ex]
\dfrac{\partial \bar{\sigma}_{ML}}{\partial \bar{\varepsilon}_{ML}^{p}} = \dfrac{\bar{\sigma}_{ML}^{(j+1)} - \bar{\sigma}_{ML}^{(j)}}{\bar{\varepsilon}_{ML}^{p,(j+1)} - \bar{\varepsilon}_{ML}^{p,(j)}}
\end{cases}
\tag{30}
$$

By re-arranging Eq. (29), the normality parameter $\dot{\lambda}$ for ML deformation mode is defined as

$$
\dot{\lambda} = \frac{F_{ML}\left(\boldsymbol{\sigma}_{(n+1)}^{(k)}, \bar{\varepsilon}_{ML,(n+1)}^{p,(k)}\right)}{\left(\dfrac{\partial \bar{\sigma}_{ML}}{\partial \boldsymbol{\sigma}}\right)_{(n+1)}^{(k)} : \boldsymbol{C}^{e} : \left(\dfrac{\partial \bar{\sigma}_{ML}}{\partial \boldsymbol{\sigma}}\right)_{(n+1)}^{(k)} + \left(\dfrac{\partial \tilde{\sigma}_{ML}^{iso}}{\partial \bar{\varepsilon}_{ML}^{p}}\right)_{(n+1)}^{(k)} - \left(\dfrac{\partial \bar{\sigma}_{ML}}{\partial \bar{\varepsilon}_{ML}^{p}}\right)_{(n+1)}^{(k)}}
\tag{31}
$$

46

The plastic strain increments are calculated using the associated flow rule for ML mode which is defined as:

$$\dot{\boldsymbol{\varepsilon}}_{ML}^{p} = \dot{\lambda}\frac{\partial\bar{\sigma}_{ML}}{\partial\boldsymbol{\sigma}}$$

(32)

For the plane stress formulation adapted in this work, at the end of each time step, the through thickness strain increment $\dot{\varepsilon}_{33}$ is calculated and reported back to the FEM code LS-DYNA using the following relationship (Abedrabbo et al. [2006])

$$\dot{\varepsilon}_{33} = \frac{(\dot{\varepsilon}_{11}^{p} + \dot{\varepsilon}_{22}^{p}) + v(\dot{\varepsilon}_{11} + \dot{\varepsilon}_{22}) - 2v(\dot{\varepsilon}_{11}^{p} + \dot{\varepsilon}_{22}^{p})}{v - 1}$$

(33)

where v is the Poisson's ratio of the material. At the end of the current time step, the updated stress state and the local effective plastic strain for ML mode are given by

$$\begin{cases} \boldsymbol{\sigma}_{(n+1)} = \boldsymbol{\sigma}_{(n+1)}^{(k+1)} \\ \bar{\varepsilon}_{ML,(n+1)}^{p} = \bar{\varepsilon}_{ML,(n+1)}^{p,(k+1)} \end{cases}$$

(34)

7.2   Reverse Compression (RC) mode

The stress update procedure for RC mode is similar to the one presented for ML deformation mode in the previous section. However, few important equations are presented here. The yielding condition for RC mode is given as

$$F_{RC}\left(\boldsymbol{\sigma}_{(n+1)}^{(k+1)}, \bar{\varepsilon}_{RC,(n+1)}^{p,(k+1)}\right) = \bar{\sigma}_{RC}\left(\boldsymbol{\sigma}_{(n+1)}^{(k+1)}, \bar{\varepsilon}_{RC,(n+1)}^{p,(k+1)}\right) - \tilde{\sigma}_{RC}^{iso}\left(\bar{\varepsilon}_{RC,(n+1)}^{p,(k+1)}\right) \leq 0$$

(35)

where k is the local iteration counter, with $k = 0$ representing the elastic trial stress state (i.e. $\boldsymbol{\sigma}_{(n+1)}^{(k=0)} = \boldsymbol{\sigma}_{(n+1)}^{trial}$ and $\bar{\varepsilon}_{RC,(n+1)}^{p,(k=0)} = \bar{\varepsilon}_{RC,(n)}^{p}$). The plastic strain increments are calculated using the associated flow rule for RC mode which is defined as

$$\dot{\boldsymbol{\varepsilon}}_{RC}^{p} = \dot{\lambda}\frac{\partial\bar{\sigma}_{RC}}{\partial\boldsymbol{\sigma}}$$

(36)

where the normality parameter $\dot{\lambda}$ is calculated as follows

$$\dot\lambda = \frac{F_{RC}\left(\boldsymbol{\sigma}_{(n+1)}^{(k)}, \bar\varepsilon_{RC,(n+1)}^{p,(k)}\right)}{\left(\frac{\partial\bar\sigma_{RC}}{\partial\boldsymbol{\sigma}}\right)_{(n+1)}^{(k)} : \boldsymbol{C}^e : \left(\frac{\partial\bar\sigma_{RC}}{\partial\boldsymbol{\sigma}}\right)_{(n+1)}^{(k)} + \left(\frac{\partial\tilde\sigma_{RC}^{iso}}{\partial\bar\varepsilon_{RC}^p}\right)_{(n+1)}^{(k)} - \left(\frac{\partial\bar\sigma_{RC}}{\partial\bar\varepsilon_{RC}^p}\right)_{(n+1)}^{(k)}} \tag{37}$$

At the end of the current time step, the updated stress state and the local effective plastic strain for RC mode are given by:

$$\begin{cases} \boldsymbol{\sigma}_{(n+1)} = \boldsymbol{\sigma}_{(n+1)}^{(k+1)} \\ \bar\varepsilon_{RC,(n+1)}^{p} = \bar\varepsilon_{RC,(n+1)}^{p,(k+1)} \end{cases} \tag{38}$$

7.3 Reverse Tension (RT) mode

The yielding condition for RT mode is written as

$$F_{RT}\left(\boldsymbol{\sigma}_{(n+1)}^{(k+1)}, \bar\varepsilon_{RT,(n+1)}^{p,(k+1)}\right) = \bar\sigma_{RT}\left(\boldsymbol{\sigma}_{(n+1)}^{(k+1)}, \bar\varepsilon_{RT,(n+1)}^{p,(k+1)}\right) - \tilde\sigma_{RT}^{iso}\left(\bar\varepsilon_{RT,(n+1)}^{p,(k+1)}\right) \leq 0 \tag{39}$$

where k is the local iteration counter, with $k = 0$ representing the elastic trial stress state. The plastic strain increments are calculated using the normality flow rule for RT mode as follows

$$\dot{\boldsymbol{\varepsilon}}_{RT}^p = \dot\lambda \frac{\partial\bar\sigma_{RT}}{\partial\boldsymbol{\sigma}} \tag{40}$$

and the normality parameter $\dot\lambda$ is given by

$$\dot\lambda = \frac{F_{RT}\left(\boldsymbol{\sigma}_{(n+1)}^{(k)}, \bar\varepsilon_{RT,(n+1)}^{p,(k)}\right)}{\left(\frac{\partial\bar\sigma_{RT}}{\partial\boldsymbol{\sigma}}\right)_{(n+1)}^{(k)} : \boldsymbol{C}^e : \left(\frac{\partial\bar\sigma_{RT}}{\partial\boldsymbol{\sigma}}\right)_{(n+1)}^{(k)} + \left(\frac{\partial\tilde\sigma_{RT}^{iso}}{\partial\bar\varepsilon_{RT}^p}\right)_{(n+1)}^{(k)} - \left(\frac{\partial\bar\sigma_{RT}}{\partial\bar\varepsilon_{RT}^p}\right)_{(n+1)}^{(k)}} \tag{41}$$

At the end of the current time step, the updated stress state and the local effective plastic strain for RT mode are given by

$$\begin{cases} \boldsymbol{\sigma}_{(n+1)} = \boldsymbol{\sigma}_{(n+1)}^{(k+1)} \\ \bar\varepsilon_{RT,(n+1)}^{p} = \bar\varepsilon_{RT,(n+1)}^{p,(k+1)} \end{cases} \tag{42}$$

7.4   Implementation framework

In the proposed constitutive model, three deformation modes (i.e. ML, RC, RT) are used to model the monotonic and reverse loading behavior of Mg alloys. At any instant throughout the deformation process, only one of the three deformation modes stays active. The yield locus for each deformation mode evolves following a reference hardening behavior and a set of evolving anisotropy/asymmetry parameters corresponding to that particular deformation mode. At the beginning of each time step, the previous stress state value $\boldsymbol{\sigma}_{(n)}$, the current strain increment $\dot{\boldsymbol{\varepsilon}}_{n+1}$ and any history variables saved at the previous stress update step are provided by the FEM code as input. The history variables include the local effective plastic strains corresponding to the three deformation modes (i.e. $\bar{\varepsilon}^p_{ML,(n)}$, $\bar{\varepsilon}^p_{RC,(n)}$, $\bar{\varepsilon}^p_{RT,(n)}$) and the prestrain $\bar{\varepsilon}^{p*}$. For each time increment, the following procedure is executed:

1. Using Eq. (4), the strain increment for the current time step is classified as either proportional (P) or reverse (R) based on the following condition:

$$\begin{cases} Proportional\ (P): & when\ \ \theta_d < \theta_r \\ Reverse\ (R): & when\ \ \theta_d \geq \theta_r \end{cases} \tag{43}$$

2. At the first time increment, the ML deformation mode is activated by default. Starting from the annealed state (i.e. $\bar{\varepsilon}^p = 0$), initial plastic deformation is bound to happen within this deformation mode. For the succeeding time steps, the current deformation mode stays as ML unless the strain increment is reverse (R) according to Eq. (43) and there is previous plastic deformation in ML mode (i.e. $\bar{\varepsilon}^p_{ML,(n)} > 0$). If both conditions are met (i.e. current increment is (R) and $\bar{\varepsilon}^p_{ML,(n)} > 0$) then the current deformation mode is either RC or RT depending on the reverse loading direction. The direction of reverse loading is either compressive or tensile and is determined by the sum of in-plane principal strain increments using Eq. (2). The current loading mode is RC if the direction of reverse loading is compressive or RT if the reverse loading direction is tensile. For subsequent time steps, the current deformation mode is the same as the previous one if the increment is proportional(P). However, if the increment is reverse (R) then the current loading mode is RT if it was RC previously or RC if it was RT previously.

3. If the current strain increment is reverse (R) and the new deformation mode is RC or RT then the local effective plastic strain corresponding to the activated deformation mode is set to zero (i.e. $\bar{\varepsilon}^p_{RC,(n)} = 0$ or $\bar{\varepsilon}^p_{RT,(n)} = 0$) and the prestrain $\bar{\varepsilon}^{p*}$ is reset to the value of the local effective plastic strain at the end of previous time step. For proportional (P) loading during RC and RT deformation modes, the previous value of the local effective plastic strain $(\bar{\varepsilon}^p_{RC,(n)}$ and $\bar{\varepsilon}^p_{RT,(n)})$ and the prestrain $\bar{\varepsilon}^{p*}$ is maintained

4. Finally, the return mapping algorithm (outlined previously) is used to update the stress state and calculate other plastic variables. At the end of each time step, the calculated stress state $\boldsymbol{\sigma}_{(n+1)}$, the incremental plastic strain $\dot{\boldsymbol{\varepsilon}}^p$, and the updated history variables are reported back to the FEM code.

Chapter 8: Constitutive Modeling Results and Discussion

8.1 Yield surface predictions for monotonic loading conditions

Figure 20 shows the evolution of subsequent yield surfaces for monotonic loading conditions corresponding to several fixed levels of the local effective plastic strains (i.e. $\bar{\varepsilon}^p_{ML} = 0\%$, 0.1%, 0.2%, ……, 9.9%, 10%) for ZEK100 and AZ31B alloys. The experimental flow stresses corresponding to uniaxial tension and uniaxial compression along RD and TD, biaxial tension and biaxial compression are also plotted as data points (symbols) for comparison.
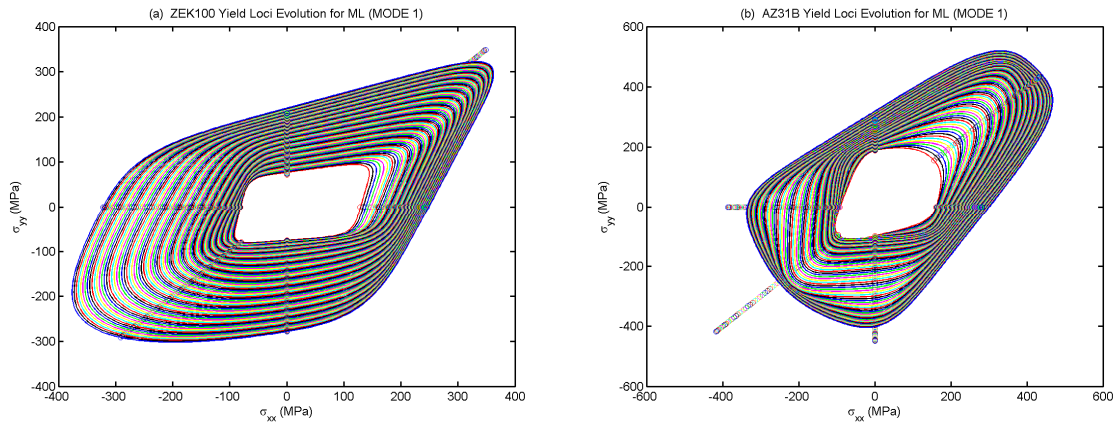
Figure 20: Yield surface evolution for monotonic loading cases (a) annealed ZEK100 and (b) annealed AZ31B sheet. The data points (symbols) represent the experimental flow stresses used for calibration of subsequent yield loci.

It is noted that, the CPB06ex2 based yield loci for ZEK100 (Figure 20 (a)) and AZ31B (Figure 20 (b)) describe well the corresponding experimental flow stresses for the plotted range of effective plastic strains of up to 10%. The developed model is able to capture the change in the shape of subsequent yield loci as a consequence of textural changes induced by the interactions between twinning and slip deformation mechanisms. Notably, the effect of $\{10\bar{1}2\}$ twinning is evident in the low compressive strengths at lower effective plastic strains (i.e. $\bar{\varepsilon}^p_{ML} \approx 0\%\text{-}1\%$) as indicated by the third quadrant strengths (i.e. the area in the third quadrant is much smaller than that in the first quadrant) in Figure 20. The shape of subsequent yield loci for ZEK100 and AZ31B are rather different owing to a relatively different starting texture leading to a comparatively different macroscopic behavior for flow hardening and plastic anisotropy. The yield loci for ZEK100 and AZ31B show a comparatively higher hardening in uniaxial compression regime as compared to

51

the tensile loading regime. Furthermore, the yield locus for ZEK100 exhibit a very strong hardening response in biaxial tension regime consistent with the experimental observations.

8.2 Yield surface predictions for reverse compression

Figure 21 and Figure 22 show the evolution of subsequent yield surfaces for reverse compression loading from different tensile prestrains $\bar{\varepsilon}_T^{p*}$ (see Table 5) for ZEK100 and AZ31B respectively. The yield loci are plotted for several fixed levels of the local effective plastic strains (i.e. $\bar{\varepsilon}_{RC}^{p} = 0\%, 0.1\%, 0.2\%, \ldots, 9.9\%, 10\%$). The experimental flow stresses used for calibration are also shown as data points (symbols) for comparison. In the present work, the loading during reverse compression occurs within the 3rd stress quadrant which is represented by solid lines in Figure 21 and Figure 22. The yield loci show a fairly accurate fit to the experimental data points for all tensile prestrain conditions corresponding to ZEK100 (Figure 21 (a-f)) and AZ31B (Figure 22 (a-f)) sheet materials. The yield surfaces for reverse compression are able to represent the experimentally observed phenomenon that a comparatively larger tensile prestrain leads to a relatively higher yield and subsequent flow stress upon reverse compression.

8.3 Yield surface predictions for reverse tension

Figure 23 and Figure 24 show the evolution of subsequent yield loci for reverse tension following different level of compressive prestrains $\bar{\varepsilon}_C^{p*}$ (see Table 6) for ZEK100 and AZ31B respectively. Similar to the previous loading cases, the yield loci are plotted for hundred fixed levels of the local effective plastic strains (i.e. $\bar{\varepsilon}_{RT}^{p} = 0\%, 0.1\%, 0.2\%, \ldots, 9.9\%, 10\%$). The reverse tension flow stresses used for calibration are also shown as data points for comparison. In the present work, the loading during reverse tension occurs within the 1st stress quadrant as represented by solid lines in Figure 23 and Figure 24. All yield loci show an accurate fit to the experimental data points for all compressive prestrain conditions and the effects of compressive prestrain on subsequent yield and hardening behavior during reverse tension is captured fairly well.

Single element finite element simulations are also performed to evaluate the response of the newly developed material model under monotonic and cyclic loading paths. The simulated results are then compared with the corresponding experimental data to verify the implementation of the

current material model and to validate its ability in capturing the hardening behavior of ZEK100 and AZ31B alloys under both monotonic and cyclic loading conditions.
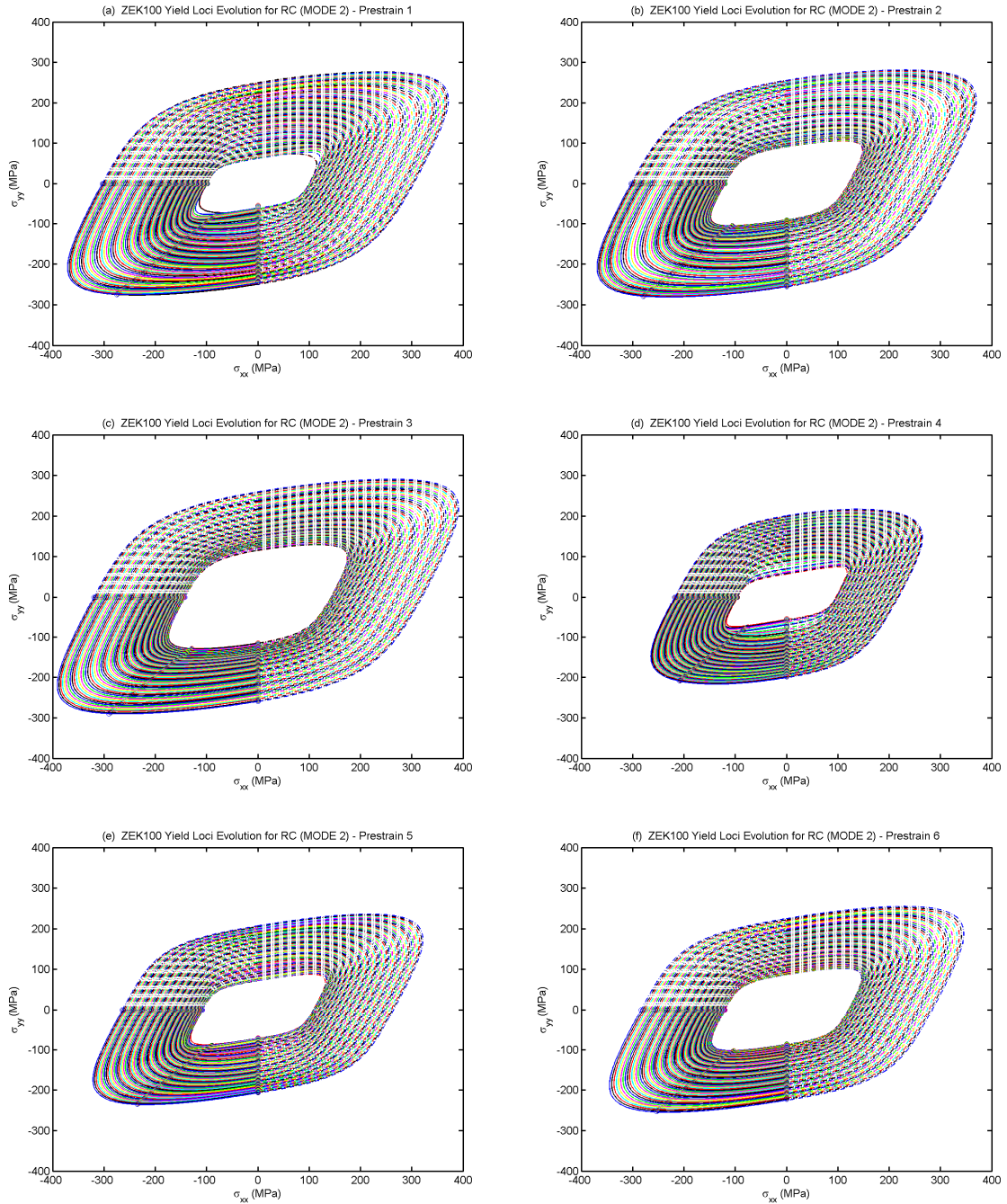
Figure 21: Yield surface evolution for anisotropic hardening during reverse compression tests of ZEK100 from different tensile prestrains (a) $\bar{\varepsilon}_T^{p*} = 0.0301$, (b) $\bar{\varepsilon}_T^{p*} = 0.0676$, (c) $\bar{\varepsilon}_T^{p*} = 0.1065$, (d) $\bar{\varepsilon}_T^{p*} = 0.0158$, (e) $\bar{\varepsilon}_T^{p*} = 0.0346$, (f) $\bar{\varepsilon}_T^{p*} = 0.0534$. The data points (symbols) represent the experimental flow stresses used for calibration of subsequent yield loci.
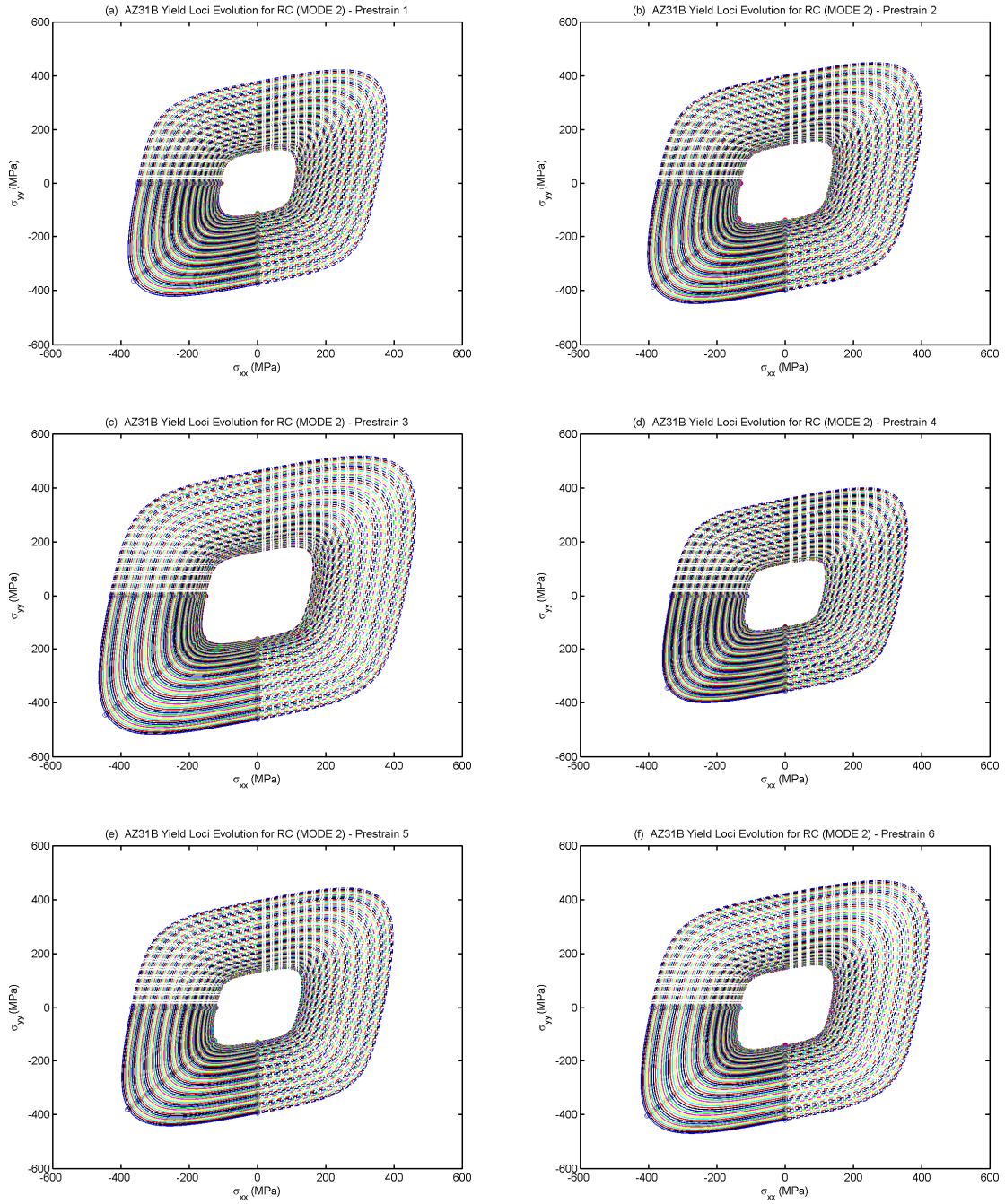
Figure 22: Yield surface evolution for anisotropic hardening during reverse compression tests of AZ31B from different tensile prestrains (a) $\overline{\varepsilon}_T^{p*} = 0.0304$, (b) $\overline{\varepsilon}_T^{p*} = 0.0671$, (c) $\overline{\varepsilon}_T^{p*} = 0.1055$, (d) $\overline{\varepsilon}_T^{p*} = 0.0154$, (e) $\overline{\varepsilon}_T^{p*} = 0.0340$, (f) $\overline{\varepsilon}_T^{p*} = 0.0526$. The data points (symbols) represent the experimental flow stresses used for calibration of subsequent yield loci.
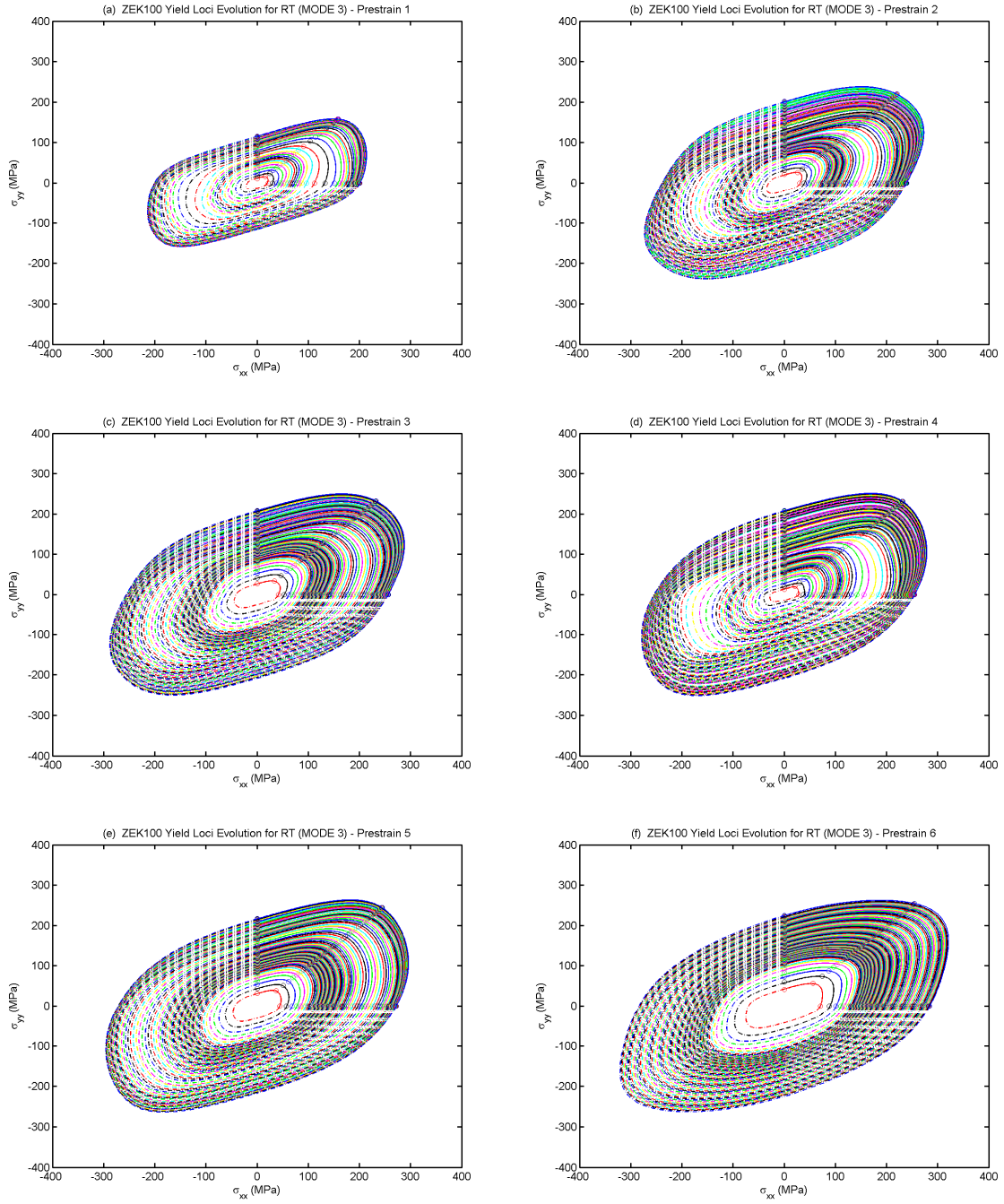
Figure 23: Yield surface evolution for anisotropic hardening during reverse tension tests of ZEK100 from different compressive prestrains (a) $\bar{\varepsilon}_C^{p*} = 0.0179$, **(b)** $\bar{\varepsilon}_C^{p*} = 0.0380$, **(c)** $\bar{\varepsilon}_C^{p*} = 0.0580$, **(d)** $\bar{\varepsilon}_C^{p*} = 0.0290$, **(e)** $\bar{\varepsilon}_C^{p*} = 0.0670$, **(f)** $\bar{\varepsilon}_C^{p*} = 0.1040$. **The data points (symbols) represent the experimental flow stresses used for calibration of subsequent yield loci.**

55

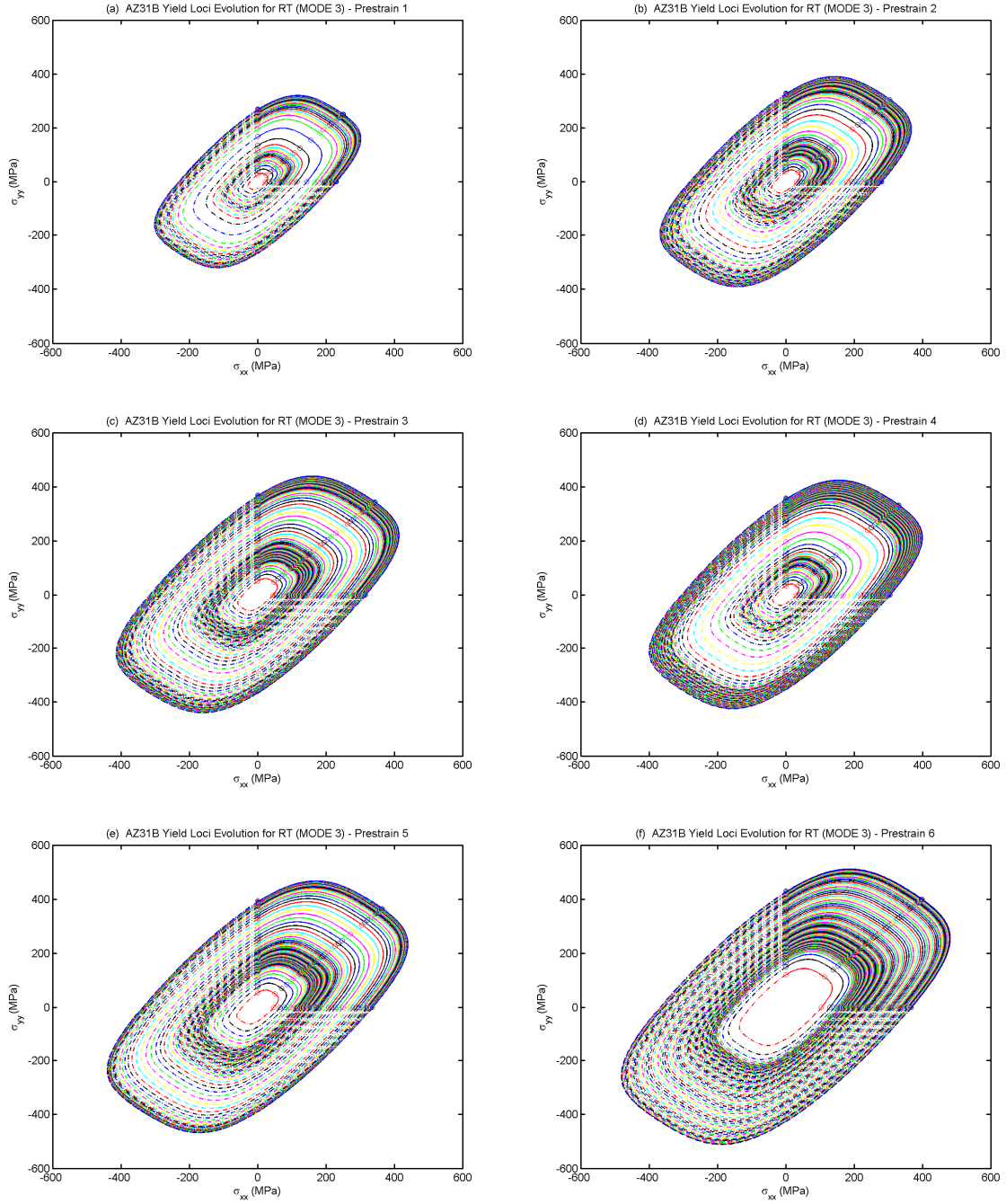**Figure 24: Yield surface evolution for anisotropic hardening during reverse tension tests of AZ31B from different compressive prestrains (a)** $\overline{\varepsilon}_C^{p*} = 0.0173$, **(b)** $\overline{\varepsilon}_C^{p*} = 0.0379$, **(c)** $\overline{\varepsilon}_C^{p*} = 0.0580$, **(d)** $\overline{\varepsilon}_C^{p*} = 0.0283$ **(e)** $\overline{\varepsilon}_C^{p*} = 0.0655$, **(f)** $\overline{\varepsilon}_C^{p*} = 0.1020$. **The data points (symbols) represent the experimental flow stresses used for calibration of subsequent yield loci.**

56

8.4   Model response to monotonic loading paths

Figure 25 shows the predictions of the proposed CPB06ex2 based material model with the experimental data for ZEK100 and AZ31B. It is noted that for all strain levels, the simulated stress-strain curves show a good agreement with the corresponding experimental results. The developed material model is able to capture the evolving flow stress anisotropy and tension-compression asymmetry and is also able to reproduce the experimentally observed concave up hardening behavior during initial in-plane compressive deformation.
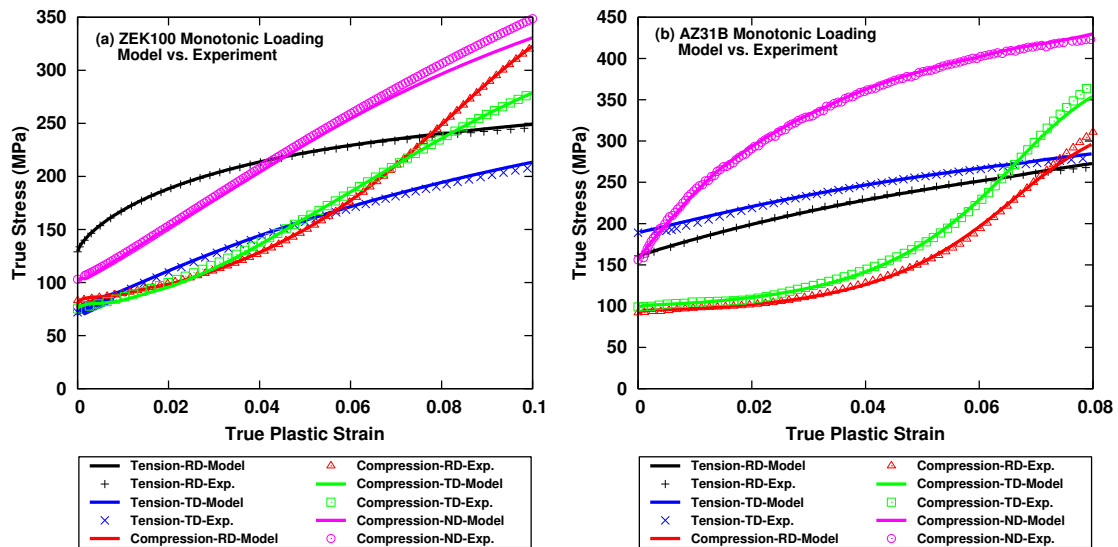
Figure 25: Comparison between simulated true stress vs. true plastic strain response and experimental data using different loading paths for (a) ZEK100 and (b) AZ31B.

The proposed model also shows a good agreement between the predicted and experimental r-values for ZEK100 (Figure 26 (a)) and AZ31B (Figure 26 (b)) sheet materials. The predicted tensile r-values for AZ31B does show a minor deviation at large experimental plastic strain of 8%. However, in general the developed model is able to capture the profound plastic anisotropy observed during in-plane tension and compression of AZ31B sheet materials.
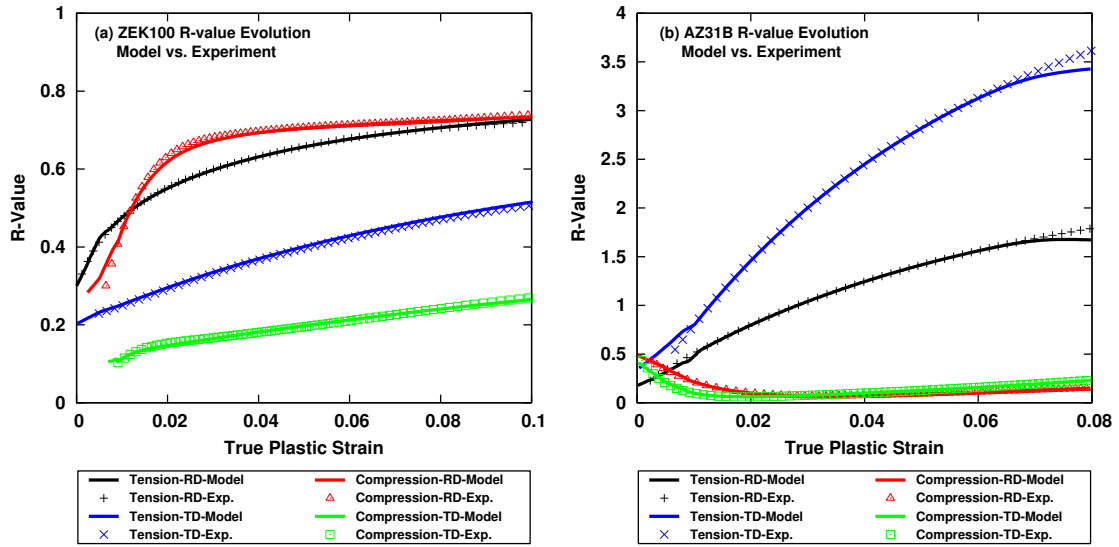
Figure 26: Comparison between simulated plastic anisotropy (r-values) response and experimental data for (a) ZEK100 and (b) AZ31B.

8.5 Model response to reverse loading paths

Figure 27 shows the model response to CTC and TCT loading paths for strain amplitudes of 2%, 4%, and 6% in RD and TD test directions of ZEK100. The proposed material model successfully reproduced the experimental large strain cyclic stress-strain curves for both RD and TD test directions of ZEK100. There are minor discrepancies between the simulated and experimental results in vicinity of stress unloading-reloading regions of cyclic curves. This may be associated with the change in effective elastic modulus which the proposed model is unable to capture. However, the proposed model is able to capture the Bauschinger effect, tension-compression asymmetry and the unusual s-shaped hardening response during reverse tension and reverse compression of ZEK100 for all the investigated cases of loading reversal in both RD and TD test directions.
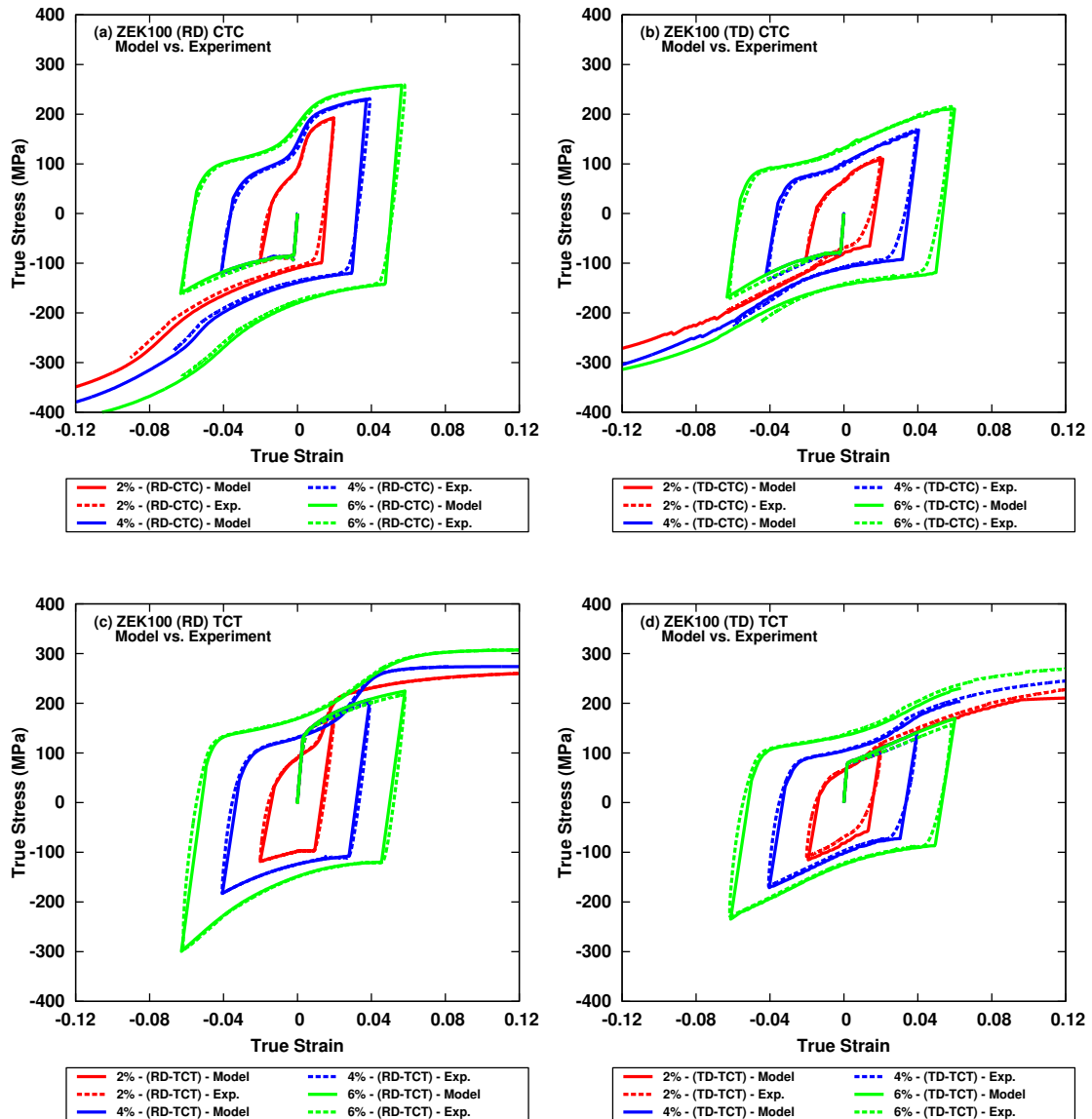
Figure 27: Comparison between simulated (a), (b) CTC and (c), (d) TCT flow stress response and experimental data for ZEK100 in RD and TD test directions.

Figure 28 shows the model response to CTC and TCT loading paths for strain amplitudes of 2%, 4%, and 6% in RD for AZ31B sheet material. For all the investigated cases of reverse loading, the simulated flow stress response shows an excellent agreement with the experimental large strain cyclic stress-strain curves for AZ31B.
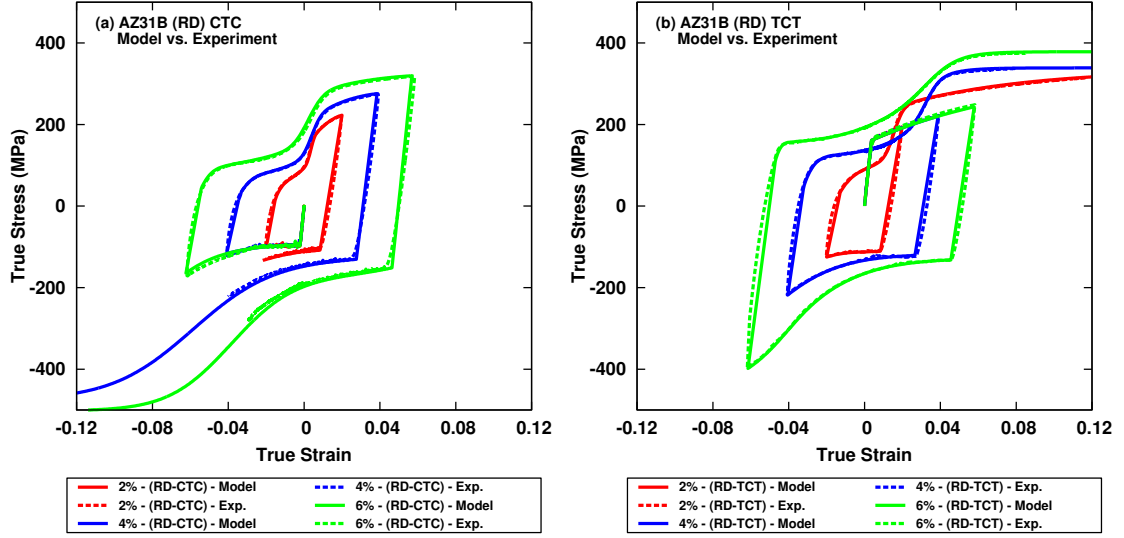
Figure 28: Comparison between simulated (a) CTC and (b) TCT flow stress response in RD and experimental data for AZ31B.

8.6   The current modelling approach and future work

The current multi-yield surface modelling approach uses multiple CPB06ex2 type evolving yield surfaces to capture the plastic anisotropy and flow stress hardening response of ZEK100 and AZ31B Mg alloys for monotonic and reverse loading paths. A rather similar approach was previously proposed by Nguyen et al. [2013] where multiple Von Mises yield surfaces were used to model the cyclic hardening behavior of AZ31B Mg sheets. Nguyen et al. [2013] suggested that the multi-yield surface approach can be regarded as a special case of the two-surface plasticity modelling approach proposed by Lee et al. [2008], where an outer stationary bounding surface and an inner expanding and translating loading surface were used to model the cyclic hardening response of AZ31B Mg sheets. In the current modelling approach, the loading surface is the current yield surface corresponding to the active deformation mode given by Eq. (15) and the stationary bounding surface can be visualized as the yield surface at an infinitely large local effective plastic strain. For the proposed model, the corresponding bounding surface for each deformation mode can be represented by the following yielding conditions

$$F_{bound} = \begin{cases} \bar{\sigma}_{ML} \; - \; \tilde{\sigma}_{ML}^{iso}\big(\bar{\varepsilon}_{ML}^{p} \; = \; \infty\big) = 0 & for\; ML\; (MODE\; 1) \\ \bar{\sigma}_{RC} \; - \; \tilde{\sigma}_{RC}^{iso}\big(\bar{\varepsilon}_{RC}^{p} \; = \; \infty\big) = 0 & for\; RC\; (MODE\; 2) \\ \bar{\sigma}_{RT} \; - \; \tilde{\sigma}_{RT}^{iso}\big(\bar{\varepsilon}_{RT}^{p} \; = \; \infty\big) = 0 & for\; RT\; (MODE\; 3) \end{cases} \qquad (44)$$

In the current work, the proposed constitutive model has been successfully applied to capture the r-values evolution and the evolving anisotropic/asymmetric flow response of HCP metals such as ZEK100 and AZ31B for monotonic as well as reverse loading (i.e. CTC and TCT) paths at room temperature. Further validation of the model for more complex proportional loading paths such as simple shear tests are in progress which will provide further information about the shape and evolution of subsequent yield loci. Furthermore, the application of the proposed model to different forming processes such as deep drawing and v-bending, is the topic for future work. Lastly, the proposed constitutive model does not account for the effects of temperature on the hardening behavior of magnesium alloys. In principle, forming of magnesium alloys is usually performed at high temperatures. Hence, it is important to include the effects of temperature into the hardening behavior of the proposed model. However, this is also left as future work.

Chapter 9: Summary and Conclusions

The monotonic and large strain cyclic behavior of AZ31B and ZEK100 magnesium alloy sheets at room temperature is studied by using a combination of mechanical and microstructural techniques. The techniques include monotonic tension, compression and large strain CTC and TCT testing along RD, DD and TD test directions, EBSD texture measurements of the annealed materials and fractography of few deformed specimens under monotonic tension and compression. Some important observations are summarized as follows

- The annealed AZ31B sheet has a very strong basal texture where the majority of crystallographic c-axes are aligned in the sheet normal (ND) direction. On the contrary, the annealed ZEK100 sheet exhibits a comparatively weak basal texture, with significant basal pole spreading in TD and a weak peak intensity as compared to annealed AZ31B sheet.

- For AZ31B sheet specimens, the monotonic yield and flow stresses are higher for in-plane loading along TD as compared to RD. The tensile flow stress curves exhibit a typical concave down shape whereas the shape of the compressive flow stress curves is concave upward (S-shape) for all in-plane loading directions. A strong tension-compression yield asymmetry is also observed for in-plane loading along the different test directions. The tension-compression yield asymmetry is higher for loading along TD as compared to RD.

- The monotonic flow characteristic of ZEK100 sheet specimens are essentially the opposite of those observed for AZ31B sheet specimens. Specifically, the monotonic yield and flow stresses are higher for in-plane loading along RD as compared to TD. The tension-compression yield asymmetry is almost negligible for in-plane loading along TD. The ZEK100 sheet specimens also exhibit a significant in-plane flow stress anisotropy when subjected to uniaxial tension.

- In general, the AZ31B sheet specimens exhibit higher flow stresses and lower ductility as compared to ZEK100 sheet specimens. The tension-compression yield asymmetry is also more pronounced in AZ31B sheet specimens as compared to ZEK100 sheet specimens and the contrary is true for the in-plane flow stress anisotropy.

- AZ31B sheet specimens show a significant evolution of r-values especially in tension. In comparison, a reduced plastic anisotropy (i.e. r-values closer to unity) is observed for ZEK100 sheet specimens

- For the in-plane large strain cyclic loading, the S-shaped hardening behavior is observed for both initial compression and reverse tension following compression regions of CTC and TCT flow curves of AZ31B and ZEK100 sheets.

In addition to the experimental characterization work, a phenomenological plasticity model has been proposed to capture the evolving anisotropic/asymmetric response of HCP metals considering monotonic and reverse loading paths. The proposed model is numerically implemented into the commercial finite element software LS-DYNA as a user material subroutine (UMAT). Experimental data for AZ31B and ZEK100 is used to obtain material parameters for the developed constitutive equations. The following observations and conclusions are made

- Even though, the observed mechanical behavior of AZ31B and ZEK100 sheets is reasonably different, the proposed model successfully captures the evolution of flow stress response and r-values under different monotonic loading conditions and test directions for both AZ31B and ZEK100 sheet materials.

- The predicted CTC and TCT results for various strain amplitudes and test directions for AZ31B and ZEK100 also showed an excellent conformity to the experimental data. In particular, the model was able to reproduce the rather different CTC and TCT hardening behavior of ZEK100 in both RD and TD test directions. In general, the model successfully reproduced the experimentally observed features such as the large cyclic tension-compression asymmetry, the Bauschinger effect and the nonlinear hardening behavior. However, minor discrepancies within the loading/unloading regions are observed.

- The proposed constitutive model is flexible enough to capture the comparatively different and complex large strain cyclic hardening behavior observed in magnesium alloys (i.e. AZ31B vs ZEK100). The proposed model can be successfully applied to simulate different sheet metal forming processes in automotive industry. However, the application of the proposed model to real forming simulations is the topic for future work.

References

Abedrabbo, N., Pourboghrat, F., Carsley, J., 2006. Forming of aluminum alloys at elevated temperatures – Part II: Numerical modeling and experimental verification. International Journal of Plasticity 22, 342–373.

Abedrabbo, N., Pourboghrat, F., Carsley, J., 2007. Forming of AA5182-O and AA5754-O at elevated temperatures using coupled thermo-mechanical finite element models. International Journal of Plasticity 23, 841–875.

Agnew, S.R., Tome´, C.N., Brown, D.W., Holden, T.M., Vogel, S.C. 2003. Study of slip mechanisms in a magnesium alloy by neutron diffraction and modeling. Scripta Materialia 48, 1003–1008.

Agnew, S.R., Duygulu, Ö., 2005. Plastic anisotropy and the role of non-basal slip in magnesium alloy AZ31B. International Journal of Plasticity 21, 1161–1193.

Agnew, S.R., Senn, J.W., Horton, J.A., 2006. Mg Sheet Metal Forming: Lessons Learned from deep drawing Li and Y Solid-Solution Alloys," JOM, 58 (5), 62-69.

Al-Samman, T., Li, X., 2011. Sheet texture modification in magnesium-based alloys by selective rare earth alloying. Mater. Sci. Eng. A 528 (10–11), 3809–22.

Armstrong, P.J., Frederick, C.O., 1966. A mathematical representation of the multiaxial Bauschinger effect. C.E.G.B. Report RD/B/N731, Berkeley Nuclear Laboratories, Berkeley, UK.

Avedesian, M. and Baker, H. (1999) Magnesium and magnesium alloys. ASM Specialty Handbook, ASM International, Metals Park, OH, USA.

Barlat, F., Lege, D.J., Brem, J.C., 1991. A six-component yield function for anisotropic materials. International Journal of Plasticity 7, 693–712.

Barlat, F., Maeda, Y., Chung, K., Yanagawa, M., Brem, J.C., Hayashida, Y., Lege, D.J., Matsui, K., Murtha, S.J., Hattori, S., Becker, R.C., Makosey, S., 1997. Yield function development for aluminum alloy sheet. Journal of Mechanics and Physics of Solids 45, 1727–1763.

Barlat, F., Brem, J.C., Yoon, J.W., Chung, K., Dick, R.E., Lege, R.E., Pourboghrat, F., Choi, S.H., Chu, E., 2003. Plane stress yield function for aluminum alloys sheets – Part I: theory. International Journal of Plasticity 19, 1297–1319.

Barnett, M.R., 2003. A Taylor Model Based Description of the Proof Stress of Magnesium AZ31 during Hot Working. Metall Mater Trans A, 34, 1799–1806.

Barnett, M.R., Keshavarz, Z., Beer, A.G., Atwell, D., 2004. Influence of grain size on the compressive deformation of wrought Mg–3Al–1Zn. Acta Mater. 52, 5093–5103.

Barnett, M.R., Nave, M.D., Bettles, C.J., 2004. Deformation microstructures and textures of some cold rolled Mg alloys. Mater. Sci. Eng. A 386, 205–211

Barnett, M.R., 2006. In: Magnesium technology 2006 symposium, San Antonio, TX.

Barrett, C.S., 1952. Structure of metals. New York: McGraw-Hill.

Bauschinger, J. 1886. On the change of the elastic limit and the strength of iron and steel, by drawing out, by heating and cooling, and by repetition of loading (summary). Minutes of Proceedings of the Institution of Civil Engineers with Other Selected and Abstracted Papers LXXXVII, p. 463.

Bettles, C.J., Gibson, M.A., 2005. Current wrought magnesium alloys: strengths and weakness. JOM 57, 46-49.

Boba, M., Worswick, M.J., Carter, J.T., Mishra, R.K., 2012. Int. Conf. on Magnesium Alloys and Their Applications, Vancouver, BC,Canada.

Boger, R.K., Wagoner, R.H., Barlat, F., Lee, M.G., Chung, K., 2005. Continuous, large strain, tension/ compression testing of sheet material. Int. J. Plast. 21 (12), 2319–2343.

Bohlen, J., Nurnberg, M.R., Senn, J.W., Letzig, D., Agnew, S.R., 2007. The texture and anisotropy of magnesium–zinc–rare earth alloy sheets. Acta Mater. 55, 2101–2112.

Bohlen, J., Yi, S., Letzig, D., Kainer, K.U., 2010. Effect of rare earth elements on the microstructure and texture development in magnesium–manganese alloys during extrusion. Mater. Sci. Eng. A 527, 7092–7098

Cazacu, O., Barlat, F., 2004. A criterion for description of anisotropy and yield differential effects in pressure-insensitive metals. Int. J. Plasticity 20, 2027–2045.

Cazacu, O., Plunkett, B., Barlat, F., 2006. Orthotropic yield criterion for hexagonal closed packed metals. Int. J. Plasticity 22, 1171–1194.

Chung, K., Shah, K., 1992. Finite element simulation of sheet metal forming for planar anisotropic metals. Int. J. Plasticity 8 (4), 453–476.

Chung, K., Richmond, O., 1993. A deformation theory of plasticity based on minimum work paths. Int. J. Plasticity 9 (8), 907–920.

Chung, K., Lee, S.Y., Barlat, F., Keum, Y.T., Park, J.M., 1996. Finite element simulation of sheet forming based on a planar anisotropic strain-rate potential. Int. J. Plasticity 12 (1), 93–115.

Doege, E., Dröder, K., 2001. Sheet metal forming of magnesium wrought alloys – formability and process technology. J. Mater. Process. Technol. 115, 14–19

Dreyer, C.E., Chiu, W.V., Wagoner, R.H., Agnew, S.R., 2010. Formability of a more randomly textured magnesium alloy sheet: Application of an improved warm sheet formability test. J. Mater. Process. Technol. 210, 37–47.

Drucker, D.C., 1949. Relation of experiments to mathematical theories of plasticity. Journal of Applied Mechanics 16, 349–357.

Duygulu, O., Agnew, S.R., 2003. The effect of temperature and strain rate on the tensile properties of texture magnesium alloy AZ31B sheet. In: Kaplan, H. (Ed.), Magnesium Technology 2003. TMS, San Diego, CA, USA, pp. 237–242

Easton, M., Song, W., Abbott, T., 2006. A comparison of the deformation of magnesium alloys with aluminum and steel in tension, bending, and buckling. Mater. Des. 27, 935–946.

Gall, S., Coelho, R.S., Muller, S., Reimers, W., 2013. Mechanical properties and forming behavior of extruded AZ31 and ME21 magnesium alloy sheets. Mater. Sci. Eng. A 579, 180–187

Ghaffari Tari, D., Worswick, M.J., Ali, U., Gharghouri, M.A., 2013. Mechanical response of AZ31B magnesium alloy: Experimental characterization and material modeling considering proportional loading at room temperature. Int. J. Plasticity 55, 247–267.

Gilles, G., Hammami, W., Libertiaux, V., Cazacu, O., Yoon, J.H., Kuwabara, T., Habraken, A.M., Duchêne, 2011. Experimental characterization and elastoplastic modeling of the quasi-static mechanical response of TA-6 V at room temperature. International Journal of Solids and Structures 48, 1277–1289.

Hantzsche, K., Bohlen, J., Wendt, J., Kainer, K.U., Yi, S.B., Letzig, D., 2010. Effect of rare earth additions on microstructure and texture development of magnesium alloy sheets. Scripta Mater. 63 (7), 725–730.

Hill, R., 1987. Constitutive dual potentials in classical plasticity. J. Mech. Phys. Solids 35, 23–33

Hill, R., 1948. A theory of the yielding and plastic flow of anisotropic metals. Proceedings of the Royal Society of London 193, 281–297.

Hill, R., 1950. Mathematical Theory of Plasticity. Clarendon Press.

Horton, J.A., Agnew, S.R., Diamond, S., Sklad, P.S., 2005b. Wrought magnesium alloy/process development. In:Wall, E., Sullivan, R., Diamond, S. (Eds.), FY 2004 Process Report for High Strength Weight Reduction Materials. US Department of Energy, Washington, DC, pp. 25–32.

Hosford, W.F., 1972. A generalized isotropic yield criterion. Journal of Applied Mechanics – Transactions of the ASME 39, 607–609.

Izadbakhsh, A., Inal, K., Mishra, R.K., Niewcza, M., 2011. New crystal plasticity constitutive model for large strain deformation in single crystals of magnesium. Comput. Mater. Sci. 50, 2185–2202.

Jain, A., Agnew, S.R., 2007. Modeling the temperature dependent effect of twinning on the behavior of magnesium alloy AZ31B sheet. Mater. Sci. Eng. A 462, 29–36.

Jiang, L., Jonas, J.J., Mishra, R.K., Luo, A.A., Sachdev, A.K., Godet, S., 2007. Twinning and texture development in two Mg alloys subjected to loading along three different strain paths. Acta Materialia 55, 3899–3910.

Jiang, L., Jonas, J.J., Mishra, R.K., 2011. Effect of dynamic strain aging on the appearance of the rare earth texture component in magnesium alloys. Mater. Sci. Eng. A 528, 6596–6605.

Kaiser, F., Bohlen, J., Letzig, D., Kainer, K.U., Styczynski, A., Hartig, C., 2003. Influence of rolling conditions on the microstructure and mechanical properties of magnesium sheet AZ31. Adv. Eng. Mater. 5, 891–896.

Kalidindi, S.R., 1998. Incorporation of deformation twinning in crystal plasticity models. J. Mech. Phys. Solids 46, 267–290

Kang, J., Wilkinson, D.S., Mishra, R.K., Embury, J.D., Essadiqi, E., Javaid, A., 2013. Microstructural Aspects of Damage and Fracture in AZ31 Sheet Materials. Journal of Materials Engineering and Performance 22(5), 1386–1395.

Kelley, E.W., Hosford, W.F., 1968a. The deformation characteristics of textured magnesium. Transactions of the Metallurgical Society of AIME 242, 654–661.

Kelley, E.W., Hosford, W.F., 1968b. Plane-strain compression of magnesium and magnesium alloy crystals. Trans. Metall. Soc. AIME 242, 5–13.

Khan, A.S., Pandey, A., Gnaupel-Herold, T., Mishra, R.K., 2011. Mechanical response and texture evolution of AZ31 alloy at large strains for different strain rates and temperatures. International Journal of Plasticity 27, 688–706.

Kim, J.H., Kim, D., Lee, Y.S., Lee, M.G., Chung, K., Kim, H.Y., Wagoner, R.H., 2013. A temperature-dependent elasto-plastic constitutive model for magnesium alloy AZ31sheets. Int. J. Plasticity 50, 66–93.

Knezevic, M., Levinson, A., Harris, R., Mishra, R.K., Doherty, R.D., Kalidindi, S.R., 2010. Deformation twinning in AZ31: Influence on strain hardening and texture evolution. Acta Materialia 58, 6230–6242

Kurkuri, S., Worswick, M.J., Bardelcik, A., Mishra, R.K., Carter, J.T., 2014. Constitutive Behavior of Commercial Grade ZEK100 Magnesium Alloy Sheet over a Wide Range of Strain Rates. Metall. Mater. Trans. A, DOI: 10.1007/s11661-014-2300-7.

Kuwabara, T., Morita, Y., Miyashita, Y., Takahashi, S., 1995. Elastic–plastic behavior of sheet metal subjected to in-plane reverse loading. In: Tanimura, S.,Khan, A.S. (Eds.), Proceedings of the Fifth International Symposium on Plasticity and its Current Applications. Gordon and Breach Publishers, Luxembourg, p. 841.

Lebensohn, R.A., Tomé, C.N., 1993. A self-consistent anisotropic approach for the simulation of plastic deformation and texture development in polycrystalsapplication to zirconium alloys. Acta Metallurgica et Materialia 41, 2611–2624.

Lee, D., Backofen, W.A., 1965. An experimental determination of the yield locus for titanium and titanium alloy sheet, Bureau of Naval Weapons Report.

Lee, M.G., Wagoner, R.H., Lee, J.K., Chung, K., Kim, H.Y., 2008. Constitutive modeling for anisotropic/asymmetric hardening behavior of magnesium alloy sheets. Int. J. Plasticity 24, 545–582.

Lee, M.G., Kim, S.J., Wagoner, R.H., Chung, K., Kim, H.Y., 2009a. Constitutive modeling for anisotropic/asymmetric hardening behavior of magnesium alloy sheets: application to sheet springback. Int. J. Plasticity 25, 70–104

Lee, M.G., Kim, J.H., Kim, D., Suh, O.S., Kim, H.Y., Wagoner, R.H., in press. Anisotropic hardening of sheet metals at elevated temperature: equipment development and validation, Exp. Mech. http://dx.doi.org/10.1007/s11340-012-9694-1.

Li, M., Lou, X.Y., Kim, J.H., Wagoner, R.H., 2010. An efficient constitutive model for room-tempearture, low-rate plasticity of annealed Mg AZ31B sheet. Int. J. Plasticity 26, 820–858.

Lou, X.Y., Li, M., Boger, R.K., Agnew, S.R., Wagoner, R.H., 2007. Hardening evolution of AZ31B Mg sheet. International Journal of Plasticity 23, 44–86.

Luque, A., Ghazisaeidi, M., Curtin, W., 2013. Deformation modes in magnesium single crystals: simulations versus experiments. Modelling and Simulation in Material Science and Engineering. 21, 045010

Maeda, Y., Yanagawa, M., Barlat, F., Chung, K., Hayashida, Y., Hattori, S., Matsui, K., Brem, J.C., Lege, D.J., Murtha, S.J., Ishikawa, T., 1998. Experimental analysis of aluminum yield surface for binary Al–Mg alloy sheet samples. International Journal of Plasticity 14, 301–318.

Mayeur, J.R., McDowell, D.L., 2007. A three-dimensional crystal plasticity model for duplex Ti–6Al–4V. International Journal of Plasticity 23, 1457–1485

Nguyen, N.T., Lee, M.G., Kim, J.H., Kim, H.Y., 2013. A practical constitutive model for AZ31B Mg alloy sheets with unusual stress–strain response. Finite Elements in Analysis and Design 76, 39-49.

Nobre, J.P., Noster, U., Kommeier, M., Dias, A.M., Scholtes, B., 2002. Deformation asymmetry of AZ31 wrought magnesium alloy. Key Eng. Mater. 230–232, 267–270.

Obara, T., Yoshinga, H., Morozumi, S., 1973. $\{11\overline{2}2\}\langle\overline{1}\overline{1}23\rangle$ slip system in magnesium. Acta Metall. Mater. 21, 845–853.

Ortiz, M., Simo, J.C., 1986. An analysis of a new class of integration algorithms for elastoplastic constitutive relations. Int. J. Numer. Meth. Eng. 23, 353–366.

Piao, K., Lee, J.K., Kim, J.H., Kim, H.Y., Wagoner, R.H., 2012a. A sheet tension/compression test for elevated temperatures. Int. J. Plasticity 38, 27–46.

Piao, K., Chung, K., Lee, M.G., Wagoner, R.H., 2012b. Twinning-slip transitions in Mg AZ31B. Metall. Mater. Trans. A 43A, 3300–3313.

Plunkett, B., Lebensohn, R.A., Cazacu, O., Barlat, F., 2006. Anisotropic yield function of hexagonal materials taking into account texture development and anisotropic hardening. Acta Materialia 54, 4159–4169.

Plunkett, B., Cazacu, O., Barlat, F., 2008. Orthotropic yield criteria for description of the anisotropy in tension and compression of sheet metals. Int. J. Plasticity 24, 847–866.

Proust, G., Tomé, C.N., Jain, A., Agnew, S.R., 2009. Modeling the effect of twinning and detwinning during strain-path changes of magnesium alloy AZ31. International Journal of Plasticity 25, 861–880.

Roberts, C.S., 1960. Magnesium and its Alloys. John Wiley, New York and London.

Reed-Hill, R.E., Robertson, W.D., 1957. The crystallographic characteristics of fracture in magnesium single crystals. Acta Metall. 5, 728–737.

Simo, J.C., Ortiz, M., 1985. A unified approach to finite deformation elastoplastic analysis based on the use of hyperelastic constitutive equations. Comput. Meth. Appl. Mech. Eng. 49, 221–245.

Simo, J.C., Hughes, T.J.R., 1998. Computational Inelasticity. Springer, New York, pp. 143–149.

Staroselsky, A., Anand, L., 2003. A constitutive model for hcp materials deforming by slip and twinning: application to magnesium alloy AZ31B. Int. J. Plasticity 19, 1843–1864.

Steglich, D., Brocks, W., Bohlen, J., Barlat, F., 2011. Modelling direction-dependent hardening in magnesium sheet forming simulations. International Journal of Material Forming 4, 243–253.

Styczynski, A., Hartig, C., Bohlen, J., Letzig, D., 2004. Cold rolling textures in AZ31 wrought magnesium alloy. Scripta Mater. 50, 943–947.

Taylor, G.I., 1938. Plastic strain in metals. J. Inst. Met. 62, 307.

Tomé, C.N., Lebensohn, R.A., Kocks, U.F., 1991. A model for texture development dominated by deformation twinning: application to zirconium alloys. ActaMetall. Mater. 39, 2667–2680.

Tome´, C.N., Lebensohn, R.A., 2004. Self-consistent homogenization methods for texture and anisotropy. In: Continuum Scale Simulation of Engineering Materials. Wiley-VCH, Weinheim, pp. 473–497.

Toros, S., Ozturk, F., Kacar, I., 2008, Review of warm forming of aluminum-magnesium alloys. Journal of Materials Processing Technology, 207, 1 – 12.

Tozawa, N., 1978. Plastic deformation behavior under the conditions of combined stress. In: Koistinen, D.P., Wang, N.-M. (Eds.), Mechanics of SheetMetal Forming. Plenum Press, New York, pp. 81–110

Ulacia, I., Dudamell, N.V., Ga´lvez, F., Yi, S., Pe´rez-Prado, M.T., Hurtado, I., 2010. Mechanical behavior and microstructural evolution of a Mg AZ31 sheet at dynamic strain rates. Acta Materialia 58, 2988–2998.

Von Mises, R., 1928. Mechanik der plastischen formanderung von kristallen. Z. Angew. Math. Mech. 8, 161–185.

Wang, H., Wu, P.D., Tomé, C.N., Wang, J., 2012. A constitutive model of twinning and detwinning for hexagonal close packed polycrystals. Mater. Sci. Eng. A 555, 93–98.

Wang, H., Wu, P.D., Wang, J., Tomé, C.N., 2013b. A crystal plasticity model for hexagonal close packed (HCP) crystals including twinning and de-twinning mechanisms. Int. J. Plasticity 49, 36–52

Wu, L., Jain, a., Brown, D.W., Stoica, G.M., Agnew, S.R., Clausen, B., Fielden, D.E., Liaw, P.K., 2008. Twinning–detwinning behavior during the strain-controlled low-cycle fatigue testing of a wrought magnesium alloy, ZK60A. Acta Mater. 56, 688–695.

Xiong, Y., Yu, Q., Jiang, Y., 2013. An experimental study of cyclic plastic deformation of extruded ZK60 magnesium alloy under uniaxial loading at room temperature. Int. J. Plasticity 53, 107–124

Xu. D.K., Liu, L., Xu, Y.B., Han, E.H., 2007. The crack initiation mechanism of the forged Mg–Zn–Y–Zr alloy in the super-long fatigue life regime. Scripta Mater 56, 1–4

Yi, S.B., Davies, C.H.J., Brokmeier, H.G., Bolmaro, R.E., Kainer, K.U., Homeyer, J., 2006. Deformation and texture evolution in AZ31 magnesium alloy during uniaxial loading. Acta Mater. 54, 549–562.

Yoo, M.H., 1981. Slip, twinning, and fracture in hexagonal close-packed metals, Metall. Trans. A 12, 409–418

Yoo, M.H., Morris, J.R., Ho, K.M., Agnew, S.R., 2002. Nonbasal deformation modes of HCP metals and alloys: role of dislocation source and mobility. Metall. Mater. Trans. A 33, 813.

Yoon, J.W., Barlat, F., Chung, K., Pourboghrat, F., Yang, D.Y., 1998. Influence of initial back stress on the earing prediction of drawn cups for planar anisotropic aluminum sheets. Journal of Materials Processing Technology, 433–437.

Yoon, J.W., Yang, D.Y., Chung, K., Barlat, F., 1999. A general elasto-plastic finite element formulation based on incremental deformation theory for planar anisotropy and its application to sheet metal forming. Int. J. Plasticity 15 (1), 35–67.

Yoon, J., Cazacu, O., Mishra, R.K., 2013. Constitutive modeling of AZ31 magnesium alloy with application to axial crushing. Mater. Sci. Eng. A 565, 203–212.

Yukutake, E., Kaneko, J., Sugamata, M., 2003. Anisotropy and non-uniformity in plastic behavior of AZ31 Magnesium alloy plates. Mater. Trans. 44 (4), 452–457.